


Development of semiempirical equation of state of binary functionally graded materials and its influence on generation of ramp compression: Comparison with bilayer graded density impactors

Aditi Ray * and Anuradha Singla *Theoretical Physics Section, Bhabha Atomic Research Centre, Mumbai - 400085, India* (Received 2 October 2020; revised 21 January 2021; accepted 25 January 2021; published 4 February 2021)

Ramp wave study involving graded impactors with discrete or continuous variation of material density is of immense interest for investigation of shock induced structural changes in solids. Hydrodynamic simulation of ramp wave generated by continuously changing functionally graded materials (FGM) requires accurate knowledge of its equation of state (EOS) parameters. However, theoretical as well as experimental EOS data for the same are not readily available. Current work is an attempt towards development of semiempirical EOS model for binary FGM (bFGM) wherein the density is a continuous function of position, either linearly or quadratically. This has been achieved by deriving analytical functions for density dependence of hughoniot parameters using the recently proposed kinetic energy average (KEA) model as well as commonly employed interpolation based methods. Six bFGMs with Al, Mg, and paraffin as low-impedance components and Cu and W as high-impedance ones are considered for the present study. It is shown that shock impedance of linear and quadratic bFGM can be expressed as superlinear/superquadratic functions of position. Subsequently, hydrodynamic simulation results of impact loading of thus constructed bFGMs on ultrathin Ta target are reported. The time profile of target pressure displayed signatures of quasi-isentropic compression (shock ramp). Ramp profiles obtained in our simulation are compared with those generated by recently reported [Phys. Rev. B **99**, 214105 (2019)] alternate material bilayer graded density impactor (blGDI) with programmable layer thicknesses. Time profile of ramp pulse is shown to have direct correlation with spatial profile of shock impedance. Influence of associated physical parameters, such as impedance of front layer material, impedance ratio of two components, impact velocity, and mixture model of EOS on shock-ramp adiabats are explored in great detail. The merits of using low and high impedance material as one component of bFGM or blGDI in lowering target heating and enhancing peak ramp pressure are investigated theoretically. Study reveals that paraffin based bFGM with quadratic density function produces the lowest temperature and entropy.

DOI: [10.1103/PhysRevB.103.054301](https://doi.org/10.1103/PhysRevB.103.054301)

I. INTRODUCTION

Investigation of material properties at extreme thermodynamic conditions is of fundamental interest to many fields dealing with high energy density physics [1,2], such as astrophysics, geophysics, inertial confinement fusion, explosive and impact driven phenomena, Z-pinch devices, and condensed matter. Large reduction in volume of condensed matter at multimegabar pressure produces substantial changes in coordination, packing, and bond distances leading to structural changes. Microstructural behavior of materials under dynamic pressures is of relevance to researchers in materials science and condensed matter physics [3].

Theoretical study of these dynamic systems requires detailed knowledge of material EOS at wide range of pressures and temperatures. EOS measurements are carried out either by shock compression of high velocity impact of flyers, lasers, current drive, or in isentropic/quasi-isentropic compression experiments (ICE) [4–6]. Recently, ICE has become the most important means to explore microstructural properties

of solids at extremely high strain rates [7]. This is due to several inherent limitations posed by shock compression. Even though shock imparts high dynamic pressure in a body, free energy of the sample comprises substantial thermal component. This irreversible thermal energy not only causes melting and vaporization of material under study but also puts an upper limit to the maximum attainable compression. In contrast, isentropic and quasi-isentropic method of dynamic compression constitutes a shockless process where moderately high pressures can be accessed with less severe temperature rise than in a shock. Another advantage of ramp compression over shock is that there is no upper limit on maximum achievable compression in the former. ICE techniques thus enable access to a wide range of pressure-temperature states located between isotherm and hughoniot. From a measurement point of view, unlike shock loading which yields single data per experiment ramp loading facilitates scanning continuum of pressure-density states along the load curve.

Isentropic experiments are being conducted using several drivers, such as multilayered GDI or continuous FGM flyer in gas gun facilities [8–10], chemical explosives [11], magnetic pulse loading [12–16], and loading by expanding plume of vapor generated by laser-ablated samples [17,18]. Laser-driven ICE is relatively new for this purpose that yielded

*Present address: Homi Bhabha National Institute, Mumbai - 400094, India; aray@barc.gov.in

several landmark results over the last decade [19–27]. More recently, laser-driven hohlraums are being used as a host for x-ray drive [28–32]. The present authors have explored the possibility of generating near-ideal isentrope in gas gun as well as high explosive (HE) driven systems by employing FGM flyers [9,33].

Each of the above methods has its characteristic time of ramp loading, e.g., pressure rise time for lasers is about a few tens of nanoseconds (ns); in magnetic loading it is about a few hundreds of ns, whereas for GDI/FGM loading in a gas gun/HE driven system it extends to about a few μ s. Several ramp wave studies involving GDI/FGM have been conducted in the past [34–37], but most of the methods have severe limitations of large entropy production, undesirable for isentropic compression [38]. Thus there is a genuine demand for enhancing peak ramp pressure associated with low entropy production in the target.

Multimaterial GDI with progressively increasing shock impedances also has the potential to enable suitable tailoring of pressure pulse [39,40]. Multilayer GDI also finds its application in an enhanced hypervelocity launcher for generating high isentropic pressures [35,41–45].

Even though fabrication of such innovative material faces technological challenges, however, the recent advancement in material technology at nanolevel has eased the manufacturing process. Currently a number of different techniques, such as stacked foils or tape casting [46,47], multimaterial lamination [48], powder compaction [49], thermal spray coating, plasma spraying [50], slip casting [51], and additive manufacturing (laser metal deposition), diffusion bonding, etc. are readily used for fabrication of FGMs with varying composition along its thickness. The concept of air plasma spraying was first demonstrated in Sandia Labs [52] for fabrication of few mm GDI by graded coating of Cu and Al onto a Cu substrate. Using this Cu-Al GDI in gas gun experiments the authors observed shock jump followed by controlled pressure rise. Livermore Lab. has reported manufacturing of GDI with individual layer widths as low as a few tens of microns [53,54]. Comprehensive review of fabrication processes and characterization of FGM can be found in Refs. [55,56].

Recently, Brown *et al.* [57] has reported fabrication of 34 μ m thick bilayer GDI using sputter deposition technique. The GDI was utilized for estimating dynamic yield strength of Ta at extremely high strain rates ($\approx 10^7$ s⁻¹). Fabricated GDI is composed of alternating layers of Al and Cu with thicknesses adjusted so as to obtain an effective density gradient through the film. We use the ramp pressure pulse generated in this experimental work as reference for validation of our simulation results and comparison with continuous FGM.

For the purpose of hydrodynamic simulation, it is straightforward to use GDI without compromising accuracy as it involves EOS of full density individual materials. However, the same is not true for continuous FGM wherein two/three different materials are mixed together in required proportion. Moreover, concentration of individual component is varied following a predecided function of layer thickness. Since theoretical or experimental data for FGM EOS are not readily available, it is necessary to accurately determine the same by taking composition variation into account.

Motivation of the current paper is to develop an accurate EOS model for two-component FGM. The proposed EOS is a mathematical and physical generalization of Mie-Grüneisen EOS (isotropic in nature) with shock hugoniot as the reference state. Anisotropic properties of FGM have been incorporated by introducing position dependent hugoniot parameters and Grüneisen gamma.

Based on known EOS parameters of constituent elements, a number of models have been developed to predict shock wave EOS of material mixtures [58,59]. Current trend in mesoscale modeling has enabled accurate prediction of EOS of binary powder mixtures [60]. We have developed a methodology for determining EOS of binary FGM as a whole. The methodology can be generalized to more than two components and to any number of layers within FGM. This has been accomplished by determining accurate EOS parameters of two-component mixtures for an adequate number of composition sets or mixture densities. In the present work, we have chosen the kinetic energy averaging based mixture model [61] as it reproduces experimental hugoniot data to a good accuracy.

Subsequently we have developed a KEA model [61] based code and determined hugoniot EOS of two-component material mixtures for nine different densities. For ease of using FGM in hydrodynamic codes, numerical data of density dependent hugoniot parameters, namely sound velocity and hugoniot slope, of three Cu based and three W based binary mixtures are fitted with suitable analytical functions. These analytical functions are then utilized for obtaining semiempirical EOS model with functionally varying hugoniot parameters for six binary FGMs, namely Al-Cu, Mg-Cu, Par-Cu, Al-W, Mg-W, and Par-W. FGM EOS of linear and quadratic density variation along thickness henceforth referred to as LFGM and QFGM, respectively, are formulated. Analytical functions are also derived for position dependent shock impedance of Cu and W based LFGM and QFGM. Although use of bFGMs for ICE is not new, there exists no systematic study on influence of spatial profile of shock impedance on ramp pulse shape.

The influence of different bFGMs (six) on ramp compression profile is investigated by performing extensive hydrodynamic simulations. For validation of our hydrodynamic model, we have implemented alternating material bilayer GDI, hereafter referred to as bGDI, with their thickness programmed in a certain manner as reported in recent experimental work [57]. In addition, we have derived the general expression for layer width of individual components in any bilayer GDI with arbitrary material combination and number of layers. This will help in selecting the material pair that would cause pressure rise in a gradual manner. Ramp pressure profiles obtained by different bFGMs are compared with analogous bGDI. Effect of low density material in bGDI/bFGM on pulse shaping has been investigated. Effect of high impedance material (Cu vs W) in bFGM/bGDI for enhancing peak pressure is also analyzed in detail. Effect of increasing impact velocity on rate of increase of pressure in the ramping zone is studied quantitatively.

Our simulation study also brings out that the EOS model plays a significant role in altering the pressure pulse shape for low velocity impact. The reason for deviation

between two models has been explained through analysis of spatial variation of shock impedance. Further, it is shown that the dependence of EOS model moderates at high velocity.

The current paper also presents thermodynamic trajectories of shock-ramp adiabats generated by different bIGDI/bFGM. The results reveal that a compression path follows the hugoniot up to the pressure generated by impact of the low impedance front layer; beyond this point the pressure-compression trajectory approaches the isentropic path. In order to examine the characteristics of isentropes produced, associated target thermodynamic parameters, e.g., maximum compression, temperature rise, and increase in entropy from ideal isentrope have been studied. It is observed that target temperature rise and entropy change for bIGDI is comparable or marginally lower than LFGM, but it is higher than that of QFGM. Additionally, our simulation brings out an important fact that for the same impact strength, peak ramp pressure can be significantly enhanced by use of W based bFGM, without appreciable escalation in target temperature and entropy, the main concern of ramp wave studies.

The paper is presented in two parts. The first part describes EOS of material mixtures and utilizes it to formulate a scheme for accurate prediction of FGM EOS. The second part is devoted for hydrodynamic simulation results of ramp compression produced by thus constructed LFGM and QFGM. Comparative analysis of bFGM results with that obtained by bIGDI of Ref. [57] are presented here. Thermodynamic properties of isentropes generated in Ta target by impact of bFGM/bIGDI are analyzed in Sec. IX. Important conclusions are summarized in Sec. X.

II. MIE-GRÜNEISEN EOS OF MATERIALS

We have implemented different EOS models, including tabular data generated by global EOS model [62] in our hydrodynamic code. However, for simplicity we have used Mie-Grüneisen analytical EOS given by

$$P = P_H + \gamma \rho (E - E_H), \quad (1)$$

where P_H and E_H , i.e., pressure and energy along hugoniot serves as the required reference state. They are determined from measured values of parameters C and S , as given below:

$$P_H = \frac{C^2(V_0 - V)}{[V_0 - S(V_0 - V)]^2}$$

$$E_H = \frac{1}{2} P_H (V_0 - V). \quad (2)$$

Parameters C and S relate hugoniot variables shock velocity U_s and particle velocity U_p by the relation: $U_s = C + S U_p$. For most of the materials this linear relationship is observed to hold well over a wide range of pressures. In Eq. (1), γ is the Grüneisen parameter and is a function of specific volume $V = 1/\rho$. For the density variation of γ we use the approximate relation: $\gamma \rho = \gamma_0 \rho_0$, where γ_0 is the Grüneisen parameter corresponding to normal density ρ_0 .

In the expansion region EOS is determined by using a simple Taylor series expanded form of Mie-Grüneisen EOS

TABLE I. Density and EOS parameters of materials used in this paper.

Material	Density (gm/cc)	C (km/s)	S	γ_0
Paraffin	0.917	3.12	1.33	1.2
Mg	1.74	4.49	1.24	1.6
LiF	2.64	5.15	1.35	2.0
Al	2.712	5.33	1.34	2.0
Cu	8.93	3.95	1.49	2.0
Ta	16.66	3.35	1.25	2.23
W	19.2	4.03	1.24	1.8

as given below:

$$P = \gamma_0 \rho_0 E + C^2(\rho - \rho_0). \quad (3)$$

Thus, EOS of any material in both compressed and expanded regions can be determined from Eq. (1) provided the values of three parameters, namely C , S , and γ_0 are known. The numerical values of these parameters for materials used in the current work are provided in Table I.

III. EOS MODELS FOR MATERIAL MIXTURE

A number of methods have been proposed to accurately describe the thermodynamic properties of multimaterial mixtures. A consolidated report on various methods can be found in Ref. [61]. Among different approaches described in that reference, the most popular one is the equilibrium-based model like averaging or interpolation method. This method relies on the assumption of pressure equilibrium between components of the mixture. Averaging methods determine unique shock hugoniot of a mixture with the knowledge of hugoniot parameters for each individual components [63,64]. In the current work we have mainly considered the kinetic energy averaging method of Ref. [61] for determining EOS of two-component mixtures leading to formulation of FGM EOS. To demonstrate the influence of EOS model on ramp compression, we have also constructed FGM EOS from interpolation based mixture model introduced by Meyers [65].

A. Method of interpolation of Meyers

According to interpolation method (IM) [65], density and hugoniot parameters of a mixture can be written as

$$\rho_{0m} = \sum_i m_i \rho_{0i}, \quad C = \sum_i m_i C_i, \quad S = \sum_i m_i S_i, \quad (4)$$

where m_i is the mass fraction of component i . For a two component mixture with constituent material densities ρ_1 and ρ_2 , first we find the mass fractions m_1 and m_2 ($m_1 + m_2 = 1$) that gives rise to a particular density ρ_0 . With these values of m_i ($i = 1, 2$), we use Eq. (4) to find C and S for that mixture. We have used this EOS model in our earlier study of FGM induced isentropic compression [9,33]. Here we will show that hugoniot parameters determined by this method have several limitations in reproducing experimental results of known mixtures.

B. Method of average kinetic energy

Next we consider the KEA model of Ref. [61] for accurate determination of shock hughoniot of mixtures. We bring out the differences of KEA method with interpolation method. We start with the assumption that initial specific volume of the mixture can be expressed as the weighted sum of the individual components, i.e.,

$$V_{0m} = \sum_i m_i V_i, \quad \sum_i m_i = 1, \quad (5)$$

where V_{0m} is the specific volume of mixture ($V_{0m} = 1/\rho_{0m}$) and m_i is the mass fraction of component i . The KEA model assumes that under pressure equilibrium particle velocity of the mixture can be expressed in terms of average particle velocity of individual components, i.e.,

$$U_{pm}^2 = \sum_i m_i U_{pi}^2. \quad (6)$$

In the above U_{pi} is the particle velocity of component i at a given pressure along its hughoniot. Equation (6) is employed to obtain mixture hughoniot from the known values of C_i and S_i . We thus adopt the following steps.

(i) For known mass fractions of constituents, initial volume and hence initial density of the mixture ρ_{0m} is calculated by using Eq. (5).

(ii) An arbitrary small equilibrium pressure P_k is chosen.

(iii) Corresponding particle velocity of the i th component is calculated by using the relation

$$U_{pi} = \frac{-C_i + \sqrt{C_i^2 + 4S_i P_k / \rho_i}}{2S_i}. \quad (7)$$

(iv) Particle velocity of mixture corresponding to hughoniot pressure P_k is then obtained using Eq. (6).

(v) Shock velocity of mixture is found using relation:

$$U_{sm} = P_k / \rho_{0m} U_{pm}.$$

(vi) The process is repeated for every small increase in equilibrium pressure P_k .

(vii) The method thus provides U_s vs U_p data for a range of pressure values for the mixture in hand. C and S of the mixture for a given composition is obtained from linear fit of U_s - U_p data.

(viii) Using mass conservation relation $\rho_{0m} U_{sm} = \rho_m (U_{sm} - U_{pm})$ we calculate final density for every U_{pm} .

(ix) Thus hughoniot of the mixture for a given composition can be determined from hughoniot of individual components.

Following the above steps we have developed a fortran program EOSMIX to determine hughoniot EOS of any multicomponent mixture. IM model based EOS is also implemented in the program. EOS of a representative mixture, i.e., Al based alloy D-16 with composition (in weight percent): Cu(4.5), Mg(1.5), Mn(0.5), Fe(0.5), Si(0.5), Zn(0.3), and rest Al has been generated using IM and KEA models. Without loss of generality, we have approximated the alloy composition as: 94% Al, 4.5% Cu, and 1.5% Mg and obtained IM and KEA model based hughoniot curves. Curves (a), (b), and (c) of Fig. 1 show the comparison of these models with experimental hughoniot data of Ref. [66]. It can be noticed that $U_s - U_p$ shock adiabat obtained from both models agree well with the experimental data. However, $P - U_p$ and $P - \rho$ curves show

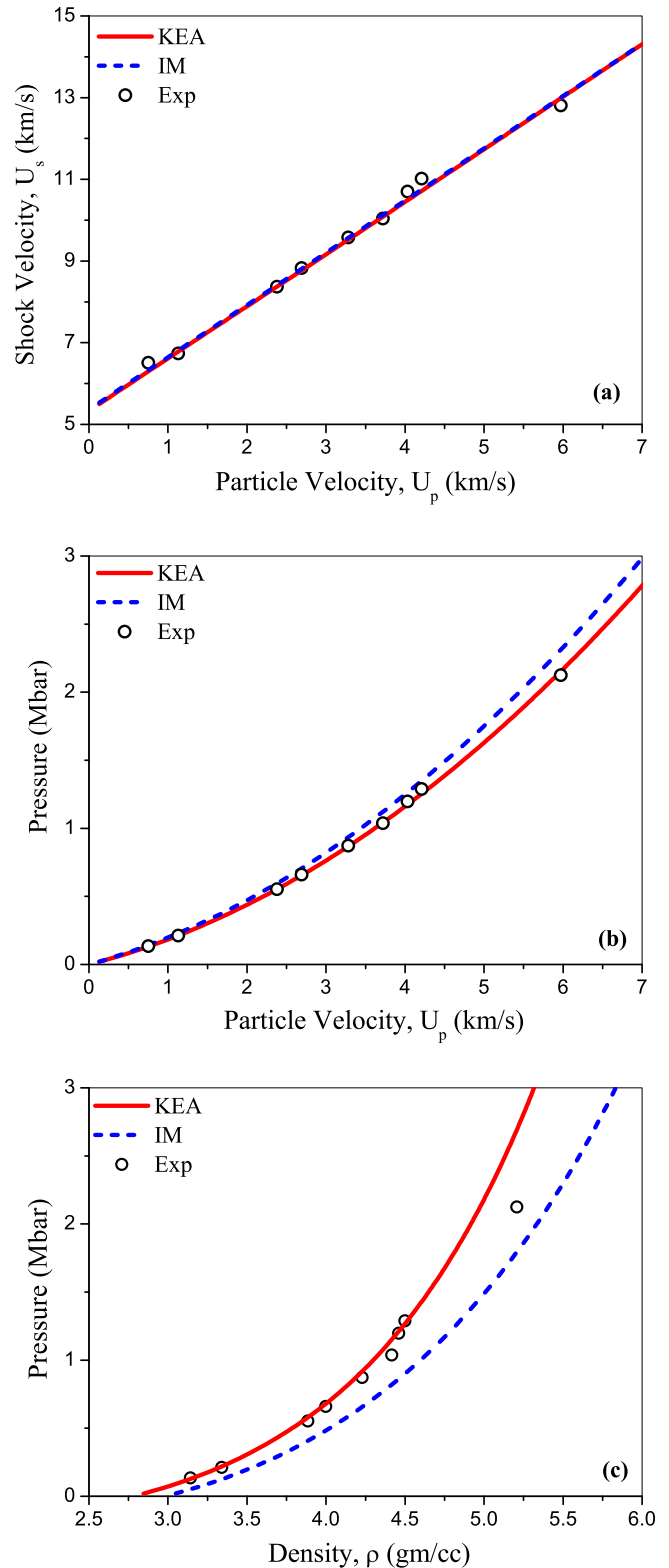


FIG. 1. Comparison of IM and KEA models with experimental hughoniot data of D-16 Al alloy: (a) shock velocity vs particle velocity, (b) pressure vs particle velocity, and (c) pressure vs density.

deviation of IM results from experiments. Mixture density C and S obtained by the two models is provided in Table II. Note that initial density predicted by interpolation method is higher than literature value of 2.78 gm/cc. It is thus obvious

TABLE II. Mixture density and EOS parameters of D-16 Al alloy obtained by KEA and IM models.

Model	Density (gm/cc)	C (km/s)	S	γ_0
KEA	2.78	5.31	1.29	1.988
IM	2.98	5.37	1.28	1.994

that the KEA model is able to determine EOS of multicomponent mixtures more accurately and proves to be superior to interpolation based method in reproducing experimental data.

IV. DETERMINATION OF GRÜNEISEN PARAMETER OF THE MIXTURE

In order to use Mie-Grüneisen EOS of the mixture in hydrodynamic code, we have adopted two different methods for determining Grüneisen gamma γ_{0m} at ambient density of mixture.

Interpolation method: According to this method [65] we have

$$\gamma_{0m} = \sum_i m_i \gamma_{0i}, \quad (8)$$

where m_i is the mass fraction of component i .

Averaging method: Grüneisen gamma at ambient density is determined by the isothermal averaging method of McQueen *et al.* [64]. According to this method we can write

$$\frac{V_{0m}}{\gamma_{0m}} = \sum_i \frac{m_i V_{0i}}{\gamma_{0i}}. \quad (9)$$

Values of γ_0 for D-16 alloy as found from two models are shown in Table II.

V. EOS OF DIFFERENT CONCENTRATION BINARY MIXTURES

FGM consists of material layers with continuously changing material densities. Herewith we deal with binary FGMs wherein layers are constructed by appropriate mixing of two elements/materials so as to get a particular density. For a given thickness, the number of FGM layers is typically very large and hence determining EOS of individual layers from first principles will be an impractical task. Here we have adopted a relatively simpler method as described below.

To illustrate the procedure we take the example of Al-Cu binary mixture. Using EOSMIX program, first we determine $U_s - U_p$ hugoniot data for nine different composition Al-Cu mixtures with concentration of Cu increased by 10 wt%. In Fig. 2 we have demonstrated $U_s - U_p$ (only KEA, IM results overlap with KEA) and $P - U_p$ hugoniot curves for pure Al, Al-20% Cu, Al-40% Cu, Al-60% Cu, Al-80% Cu, and pure Cu. Difference in results between the two models are quite apparent in curve Fig. 2(b).

In each case $U_s - U_p$ data has been fitted with a straight line to obtain C and S for that compositions. Figures 3(a) and 3(b) illustrate the density (composition) variation of EOS parameters for Al-Cu mixture as obtained by fittings of KEA and IM results. It is clear that hugoniot intercepts, i.e., C [red symbols of Fig. 3(a)] obtained by two models differ significantly, whereas hugoniot slopes match to a good extent.

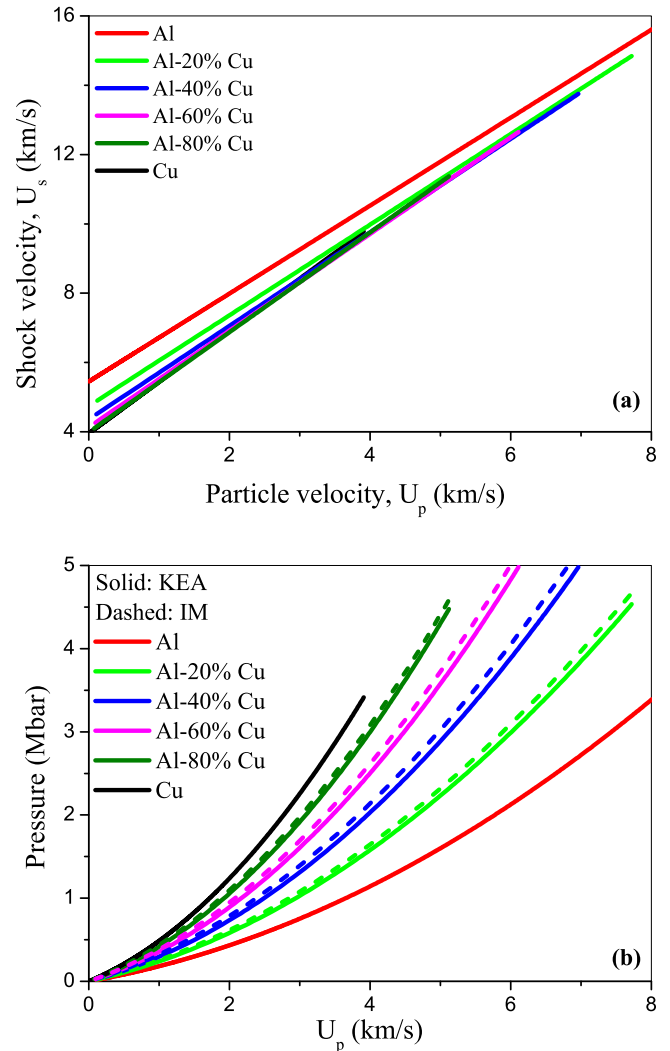


FIG. 2. Hugoniot curves of different composition Al-Cu mixtures: (a) shock velocity vs particle velocity (KEA model) and (b) pressure vs particle velocity. Solid and dashed lines refer to results pertaining to KEA and IM models, respectively.

For the purpose of predicting EOS of graded layers like FGM, we need C and S as a continuous function of layer density. To that end, our next step was to fit these 11 sets of C and S data with a suitable analytical function of density. C vs ρ and S vs ρ fittings for KEA and IM models are demonstrated by solid and dashed lines of Fig. 3. Analytical functions describing variation of C and S with ρ are provided in Table III. It can be noticed that even though in both the models C decreases with density, their functional forms are quite different. These functions serve a good purpose for predicting hugoniot parameters of any composition of a given mixture for which experimental data are not available.

A. EOS of varying composition Mg-Cu and paraffin-Cu mixtures

Density dependence of EOS parameters has been extended for two other Cu based mixtures, namely Mg-Cu and

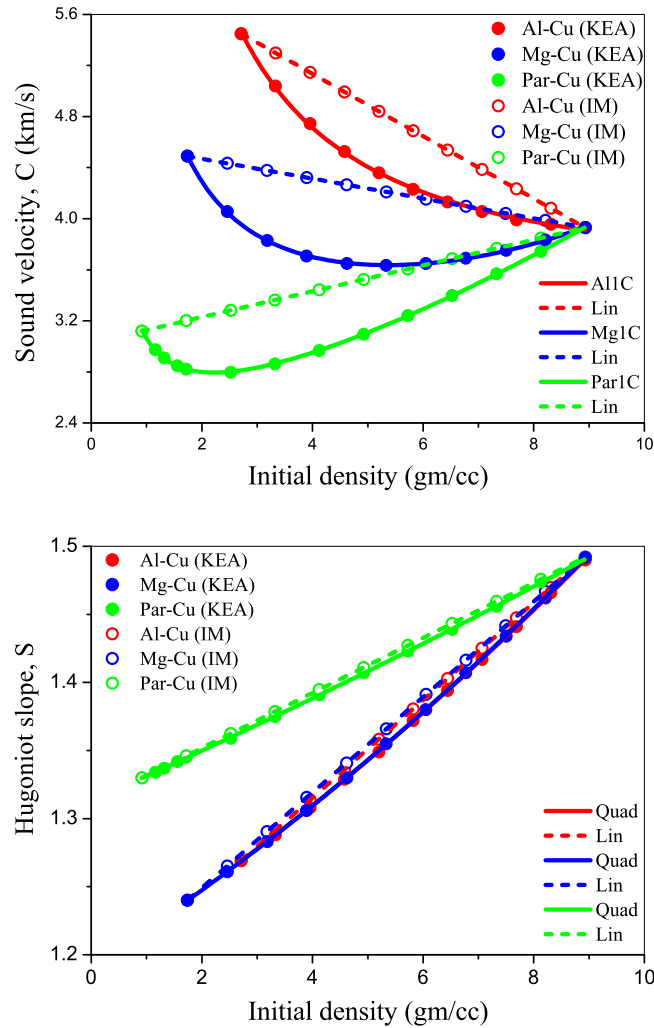


FIG. 3. Density variation of sound velocity C and hughoniot slope S of Cu based mixtures. Filled and open circles in each case refer to data calculated using KEA and IM models, respectively. Solid and dashed lines represent best fitted curves.

paraffin-Cu (Par-Cu). There are reports of employing Mg-Cu FGM as a part of wide range GDI in gas gun experiments [67], but to the best of our knowledge use of Par-Cu combination for ICE is not reported so far.

Following the methodology described for the Al-Cu system, we have determined C and S (as a function of ρ) for

TABLE III. KEA and IM model based C vs ρ and S vs ρ fitting functions for Al-Cu, Mg-Cu, and Par-Cu binary mixtures. All linear functions have the general form: $a + b\rho$, and all quadratic functions are of the form: $a + b\rho + c\rho^2$.

Mix.	Model	$C(\rho)$: Function	$S(\rho)$: Function
Al-Cu	KEA	$a + b/\rho + c\rho$: Allc	Quadratic
	IM	Linear	Linear
Mg-Cu	KEA	$a\rho^3 + b/\rho + c\rho + d$: Mg1c	Quadratic
	IM	Linear	Linear
Par-Cu	KEA	$a\rho^2 + b/\rho + c\rho + d$: Par1c	Quadratic
	IM	Linear	Linear

Mg-Cu and Par-Cu mixtures as shown by blue and green symbols (filled circle for KEA and open circle for IM) of Fig. 3. Corresponding fitting functions are shown by solid and dashed lines. The interesting point to observe is that there exists no general pattern for C among different mixtures. Thus it is necessary to develop $C(\rho)$ and $S(\rho)$ functions of the binary FGM in hand before employing it.

Further, sound velocities of Mg-Cu and Par-Cu exhibit a minimum at certain density when calculated by KEA model, but IM model does not predict such a minimum for any mixtures. Variation of S with density for all three compositions is linear for the IM method, but quadratic function best fits the KEA results. Consolidated outcome of the fitting functions for Al-Cu, Mg-Cu, and Par-Cu binary mixtures are listed in Table III with the corresponding fitting coefficients provided in Table IV.

B. EOS of W based binary mixtures with paraffin, Mg, and Al as other component

Like in the case of shock loading, enhancement in peak isentropic pressure can be realized by increasing impedance of rear end material of FGM. As spread of bulk sound velocities among different structural materials is not very wide, the only possibility to enhance impedance is to use high density material at the rear end. This can be illustrated by observation that acoustic impedance (Z_0) of Cu is about $3.52 \text{ gm/cm}^2/\mu\text{s}$, which is much lower than W ($Z_0 = 7.734 \text{ gm/cm}^2/\mu\text{s}$), even though sound velocity of the two is very close ($\approx 4 \text{ km/s}$).

Fabrication of Al-W FGM with varying Al concentration has been reported in Ref. [68]. Shock compression behavior of Al-W binder granular mixtures has been studied recently by mesoscale simulation [69]. However, we have not come across any shock/ramp wave experiment employing Al-W FGM. Mg-W FGM has been manufactured from stacked metal powder layers and one-step hot-pressure sintering [70]. The authors have shown that impact of Mg-W FGM results in generation of shock-ramp feature in particle velocity profile. However, the number of layers used in their mm size impactor is restricted to 12 reaching a maximum density of 5 gm/cc .

In this section, we thus determine EOS parameters of three W based binary mixtures. Like in the case of Cu based mixtures, paraffin, Mg, and Al serve as low impedance component. For each of these cases hughoniot data for different mass fractions giving rise to different mixture density have been generated by using EOSMIX program. The resulting C and S data for nine mixtures along with pure materials are shown in Figs. 4(a) and 4(b). Also shown in the figures are corresponding fitted curves with functions given in Table V. Numerical values of fitting coefficients are listed in Table VI.

It can be seen from Fig. 4 that for all three W based systems C reduce with increase in ρ up to certain mixture density, thereafter it increases. However, unlike Cu based systems S decreases as density increases. Our results of C for Par-W mixtures containing 8.9% and 19.2% W by volume show reasonably good agreement with experimental data (Ref. [71]) as shown in Fig. 4.

Our C vs ρ data for the Mg-rich Mg-W system agree well with ‘AWE’ results of Ref. [72], but it deviates for the W-rich mixture. Moreover, ‘AWE’ method predicts minimum

TABLE IV. Fitting coefficients of $C(\rho)$ and $S(\rho)$ functions introduced in Table III.

Mix.	Model	$C(\rho)$			$S(\rho)$			
		a	b	c	d	a	b	c
Al-Cu	KEA	2.99	6.55	2.1×10^{-2}		1.19	2.6×10^{-2}	8.4×10^{-4}
	IM	6.11	-0.24			1.17	3.6×10^{-2}	
Mg-Cu	KEA	6.2×10^{-4}	2.88	4.7×10^{-2}	2.75	1.19	2.6×10^{-2}	8.6×10^{-4}
	IM	4.63	-7.8×10^{-2}			1.18	3.5×10^{-2}	
Par-Cu	KEA	5.8×10^{-3}	0.85	0.15	2.05	1.31	1.8×10^{-2}	2.2×10^{-4}
	IM	3.03	0.10			1.31	2.0×10^{-2}	

sound velocity for 10 wt% Mg plus W mixture, i.e., at 10 gm/cc, which is unphysical. On the other hand, Batsanov formulation [63] does not lead to any extremum in the C vs ρ curve. This indicates that hugoniot parameters for the Mg-W mixture are very sensitive to the model used.

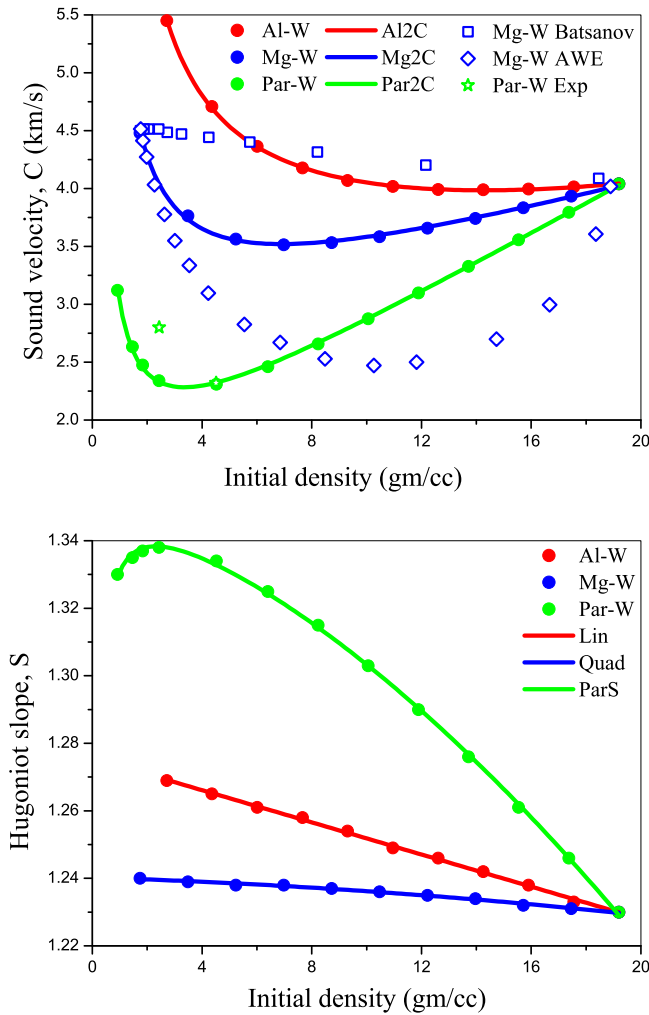


FIG. 4. Density variation of C and S of W based mixtures. Filled circles in each case refer to calculated data employing the KEA model. Solid lines represent the best fitted curves as listed in Table V. The green asterisk represent experimental data for two densities of Par-W mixture [71]. Open diamond (blue) and open squares (blue) belong to Mg-W mixture data taken from Ref. [72] obtained by AWE and Batsanov formulations.

Sections VA and VB display an interesting feature of KEA model, i.e., a mixture can have a lower sound velocity than either of the components. The condition under which this feature can be observed has been established by Torvik [73]. According to that work, minimum in sound velocity vs mixture density curve occurs if the following inequalities are satisfied:

$$\begin{aligned}
 2A \leq B \leq 2A/(1-A) &: \text{ for } A < 0 \text{ and } B < 0, \\
 2A \leq B \leq 2A/(1-A) &: \text{ for } 0 < A < 1 \text{ and } B > 0, \\
 B \geq 2A &: \text{ for } A > 1, B > 0.
 \end{aligned} \tag{10}$$

The parameters A and B in Eq. (10) are defined below:

$$A = \frac{\rho_1}{\rho_2} - 1, \quad B = \left(\frac{Z_1}{Z_2}\right)^2 - 1, \tag{11}$$

with ρ_1, Z_1 and ρ_2, Z_2 as density and shock impedance of the two components involved.

Further, if A and B are of unlike signs, then no extremum value can occur. Applying these conditions, we find that C for all mixtures considered in the present work should show a minimum at certain density. A minimum of C can be observed for all the cases shown in Fig. 3 and Fig. 4 for KEA data. IM or other averaging models either do not exhibit such extremal feature or predict extremum at a density not acceptable from a compressibility point of view. This justifies considering the KEA model for developing accurate EOS of FGM.

VI. PREDICTING EOS OF BINARY FGMs

Having found the smooth functions for density variation of hugoniot parameters for three Cu based and three W based binary mixtures, we use them for generating empirical EOS for FGM plates. Following our previous work [9,33], we introduce two types of FGM, i.e., LFGM and QFGM wherein layer density along the thickness varies linearly or quadratically

TABLE V. C vs ρ and S vs ρ fitting functions for Al-W, Mg-W, and Par-W binary mixtures based on the KEA model.

Mix.	$C(\rho)$: Function	$S(\rho)$: Function
Al-W	$a\rho^2 + b/\rho + c$: Al2C	$a + b\rho$: Linear
Mg-W	$a\rho + b/\rho + c$: Mg2C	$a\rho^2 + b\rho + c$: Quadratic
Par-W	$a/\rho + b\rho + c$: Par2C	$a\rho^2 + b/\rho + c\rho + d$: ParS

TABLE VI. Fitting coefficients of $C(\rho)$ and $S(\rho)$ as introduced in Table V.

Mix.	$C(\rho)$			$S(\rho)$			
	a	b	c	a	b	c	d
Al-W	9.56×10^{-4}	5.56	3.40	1.28	-2.38×10^{-3}		
Mg-W	6.39×10^{-2}	3.03	2.64	-1.53×10^{-5}	-2.53×10^{-4}	1.24	
Par-W	1.50	0.13	1.39	-1.57×10^{-4}	-2.29×10^{-2}	-3.62×10^{-3}	1.36

with position. Mathematically we express them by Eq. (12) and Eq. (13), respectively.

$$\rho(x) = \rho_1 + \frac{\Delta\rho}{\Delta x}(x - x_1), \quad (12)$$

$$\rho(x) = \rho_1 + \frac{\Delta\rho}{(\Delta x)^2}(x - x_1)^2. \quad (13)$$

In the above $\Delta\rho = \rho_2 - \rho_1$, $\Delta x = x_2 - x_1$, $\rho_1 = \rho(x = x_1)$, and $\rho_2 = \rho(x = x_2)$. Having known the position dependence of density, we employ C vs ρ and S vs ρ fitting functions derived in Sec. VA and Sec. VB to determine the spatial variation of C and S within a particular type of binary FGM. In general, we can write

$$C(x) = f[\rho(x)], \quad S(x) = g[\rho(x)]. \quad (14)$$

Similarly, position dependence of acoustic and shock impedances of bFGM under consideration can be expressed as

$$\begin{aligned} Z_0(x) &= \rho(x)C(x) \\ Z_s(x) &= \rho(x)U_s(x) \\ &= \rho(x)[C(x) + S(x)U_p]. \end{aligned} \quad (15)$$

In order to generate $C - x$, $S - x$, and $Z_s - x$ data for two types of FGM, we have introduced an EOS module for bFGM in our 1D hydrodynamics code. The module contains semiempirical functions of density dependence of C and S for six binary mixtures discussed above. Since for LFGM, layer density is directly proportional to position, the functional dependence of C and S on spatial points x will be the same as the density dependence and hence not shown separately. However, deviation in spatial dependence of C and S from that of density dependence is expected for QFGM. Spatial variation of sound velocity for six different binary QFGMs (width $34 \mu\text{m}$) are shown in Fig. 5. Solid lines are obtained by using KEA model based fitting functions. To demonstrate the influence of EOS models, IM fitting functions are presented for Cu based QFGMs (dashed lines). Since hughoniot slope S does not vary significantly with density, we have not shown them explicitly, but HYDRO code takes this into account.

A. Spatial variation of shock impedance for binary FGM

The purpose of employing FGM is to induce successive weak shocks so as to increase the pressure slowly. This can be achieved by the impact of flyers with continuously increasing shock impedance from one end to the other.

Shock impedance for Al-Cu, Mg-Cu, and Par-Cu FGMs calculated from Eq. (14) are shown in Fig. 6. Four panels refer

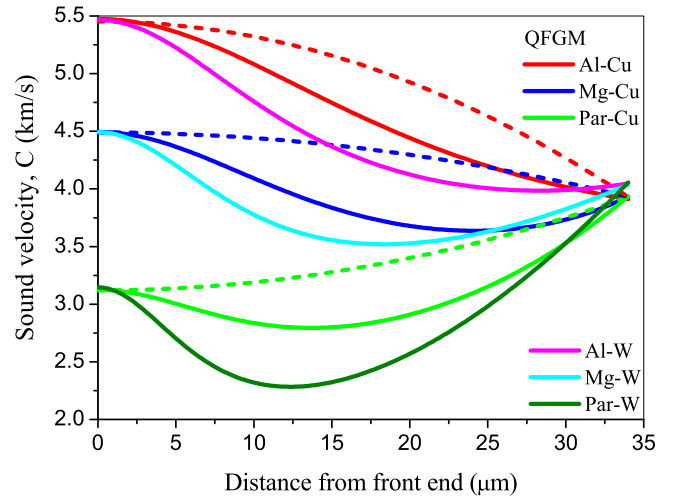


FIG. 5. Spatial variation of sound velocity for Cu and W based binary QFGM. Solid lines are the results of KEA scheme and dashed lines correspond to IM results for three Cu based QFGMs.

to four different constant particle velocity cases: $U_p = 0, 0.5, 5.0, 10.0$ km/s. $U_p = 0$ corresponds to acoustic impedance Z_0 . The effect of two different EOS models is illustrated by solid (KEA) and dashed (IM) curves. It can be easily noticed that difference between Z_s estimated by two models is maximum for $U_p = 0$ and gradually diminishes as particle velocity is increased. Nevertheless, Z_s vs x profile for both the models turns out to be the same. Spatial variation of shock impedance for three W based FGMs (width $34 \mu\text{m}$) is displayed in Fig. 7. An interesting point to note from Fig. 6 and Fig. 7 is that Z_s vs x profiles are quite different from C vs x profiles (Fig. 5), even for $U_p = 0$. Thus the general assumption made in almost all analytical and numerical work on graded density materials that *all physical properties, like sound velocity, acoustic impedance, Young's modulus, etc., follow the same function as mass density* [74–76] is in gross disagreement when it comes to bFGMs.

To establish the functional dependence of Z_s with x , we have fitted the data with a general power law variation. We express Z_s with an analytic function of normalized position given below:

$$Z_s(x) = Z_1 \left[1 + (Z_R - 1) \left(\frac{x}{D} \right)^m \right]. \quad (16)$$

In the above equation $D = 34 \mu\text{m}$ is the width of the FGM plate. Fitting constants Z_1 and Z_R are equivalent to shock impedance of low density front layer and shock impedance ratio of rear and front end layers. Values of Z_R and nonlinear exponent m for all the above cases are provided in Table VII. The functional form of position dependence of shock impedance given by Eq. (16) is analogous to the one used by Bruck [74] for continuous FGM. But the author had assumed the same functional form for volume fraction as well as sound velocity, which is not universally true.

It can be observed from Table VII that as per KEA scheme, linear variation of density with position (LFGM) gives rise to superlinear dependence ($m > 1$) of Z_s with x . Similarly Z_s vs x curve is superquadratic ($m > 2$) for QFGM. Moreover, except

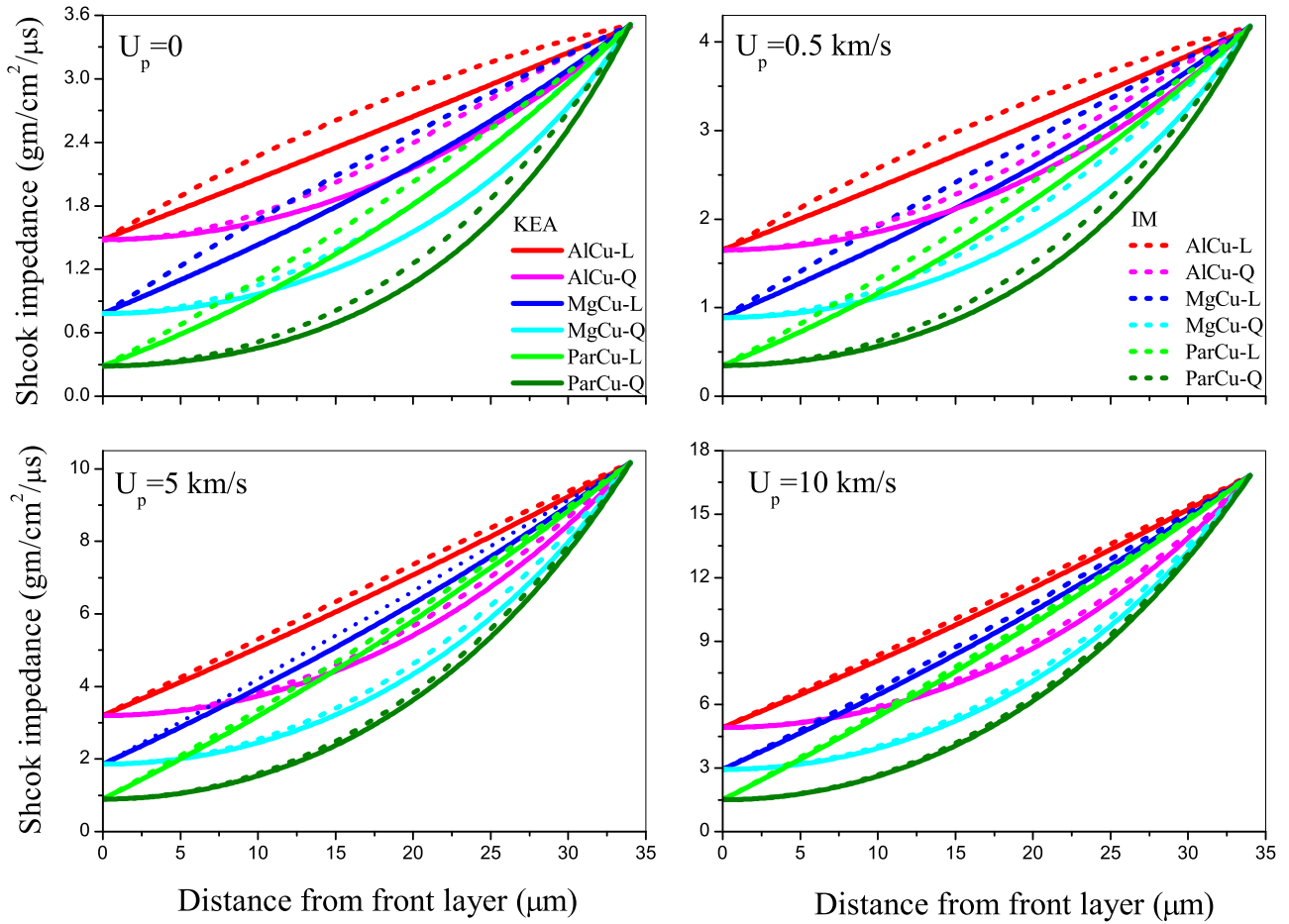


FIG. 6. Spatial variation of shock impedance of three Cu based binary FGMs. Four panels display Z_s for four different U_p values. Each panel shows Z_s for Al-Cu, Mg-Cu, and Par-Cu FGM with linear (red, blue, and green lines) and quadratic (magenta, cyan, and olive lines) density functions. In each case KEA and IM based results are shown by solid and dashed curves, respectively.

for AlCu-L and AlCu-Q cases the magnitude of exponent m shows a downward trend with U_p .

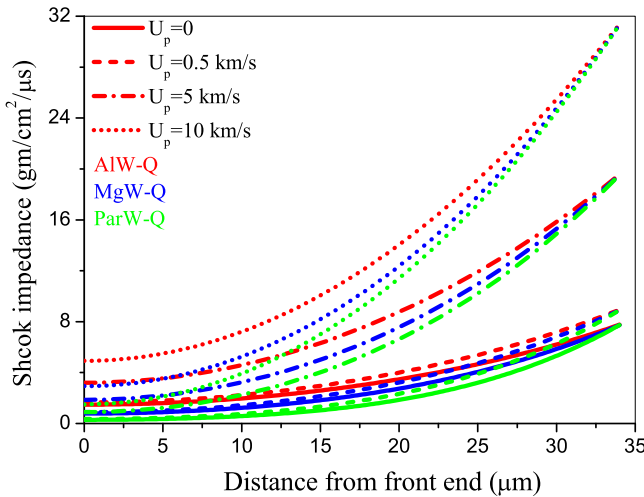


FIG. 7. Spatial variation of shock impedance of three W based QFGMs. Solid, dashed, dash-dot, and dotted lines in each case correspond to constant particle velocity of $U_p = 0, 0.5, 5.0, 10.0$ km/s. All results are based on the KEA mixture model of EOS.

In contrast, spatial variation of Z_s in the IM scheme is sublinear and subquadratic for Al-Cu and Mg-Cu FGM of both types, except at very high U_p . The effect of these lower values of m on ramp profiles will be studied in Sec. VIII E. It can also be noticed that at low velocity, the value of m for a particular composition W based FGM is more than the corresponding Cu based FGM. For example, $m = 2.81$ for Par-W QFGM when $U_p = 0.5$ km/s, whereas $m = 2.61$ for Par-Cu QFGM indicating a slower rise of pressure. The trend is reversed at higher velocities. In Fig. 8 we have compared the values of m for various FGM cases. A large spread in m values among six FGMs can be observed at low U_p . This causes significant variation in pressure profile in the ramping zone as discussed in Sec. VIII D. For higher U_p , m values converge to a narrow band of $1 < m < 1.2$ for LFGM and $2 < m < 2.3$ for QFGM. Position dependent shock impedance is responsible for creating a gradual rise of pressure and hence plays a significant role in providing shape of ramping pulse. Although this is not new, our study provides quantitative explanation for the same.

Table VII also shows an increasing trend of Z_R with particle velocity. Moreover, for a particular U_p , Z_R is more for lower values of ρ_1 , i.e., $Z_R^{\text{Al-Cu}} < Z_R^{\text{Mg-Cu}} < Z_R^{\text{Par-Cu}}$. Also Z_R is higher for larger values of ρ_2 , i.e., $Z_R^{\text{Al-W}} > Z_R^{\text{Al-Cu}}$ and so on.

TABLE VII. Fitting coefficients of Eq. (16) for different binary FGMs at $U_p = 0, 0.5, 5.0,$ and 10.0 km/s.

Binary FGM	Model	U_p							
		0		0.5		5.0		10.0	
		Z_R	m	Z_R	m	Z_R	m	Z_R	m
AlCu-L	KEA	2.35	1.03	2.49	1.05	3.10	1.10	3.32	1.11
	IM	2.62	0.71	2.72	0.78	3.21	0.97	3.40	1.03
AlCu-Q	KEA	2.35	2.05	2.50	2.08	3.12	2.16	3.36	2.18
	IM	2.51	1.55	2.64	1.64	3.20	1.96	3.41	2.05
MgCu-L	KEA	4.09	1.25	4.29	1.23	5.04	1.18	5.30	1.17
	IM	4.74	0.90	4.86	0.93	5.35	1.05	5.52	1.08
MgCu-Q	KEA	4.24	2.40	4.44	2.37	5.22	2.29	5.48	2.27
	IM	4.63	1.83	4.79	1.89	5.40	2.08	5.61	2.13
ParCu-L	KEA	9.58	1.41	9.53	1.36	9.67	1.19	9.79	1.15
	IM	10.67	1.16	10.56	1.15	10.28	1.11	10.22	1.10
ParCu-Q	KEA	10.60	2.71	10.50	2.61	10.39	2.32	10.40	2.25
	IM	11.36	2.28	11.21	2.25	10.77	2.19	10.65	2.17
AlW-L	KEA	4.96	1.10	5.15	1.09	5.99	1.02	6.33	1.01
AlW-Q	KEA	5.08	2.16	5.26	2.13	6.05	2.03	6.35	2.01
MgW-L	KEA	8.60	1.23	8.80	1.20	9.78	1.08	10.20	1.05
MgW-Q	KEA	9.13	2.40	9.31	2.34	10.11	2.14	10.42	2.08
ParW-L	KEA	18.14	1.55	17.32	1.45	17.98	1.13	19.59	1.04
ParW-Q	KEA	21.04	3.01	20.16	2.81	19.61	2.23	20.11	2.08

B. Shock impedance ratio of binary FGM components

The shock impedance ratio is an important parameter for maximizing peak ramp pressure. In Fig. 9 we have displayed the ratio $Z_R = Z_2/Z_1$ (actual) as a function of increasing U_p . It can be observed that except for paraffin based mixtures, for all other cases Z_R initially increases with U_p , reaches a maximum value specific to the binary composition in hand, and then rises very slowly for further increase of U_p . For the two paraffin based FGMs the value of Z_R shows initial rapid decline followed by slower decrease. The near-saturation-like feature of impedance ratio can be understood from the following derivation.

$$Z_R = \frac{\rho_2 U_{s2}}{\rho_1 U_{s1}} = \frac{\rho_2 (C_2 + S_2 U_p)}{\rho_1 (C_1 + S_1 U_p)} \quad (17)$$

First we consider the case when impact velocity is such that $S_1 U_p \gg C_1$. Equation (17) can be rewritten as

$$\begin{aligned} Z_R &= \frac{\rho_2 S_2 (1 + C_2/S_2 U_p)}{\rho_1 S_1 (1 + C_1/S_1 U_p)} \\ &= \frac{\rho_2 S_2}{\rho_1 S_1} \left[1 + \frac{1}{U_p} (C_2/S_2 - C_1/S_1) \right] \\ &\approx \frac{\rho_2 S_2}{\rho_1 S_1} \left[1 + \frac{1}{U_p} C_2/S_2 \right]. \end{aligned} \quad (18)$$

If $U_p \gg C_2$, i.e., for hypervelocity impact Eq. (18) reduces to $Z_R = \rho_2 S_2 / \rho_1 S_1$ making Z_R independent of velocity. For most of the materials S is close to 1, hence the maximum value of Z_R is approximately equal to the density ratio.

For low velocity impact, i.e., $S_1 U_p \ll C_1$, Eq. (17) can be rearranged as

$$Z_R = \frac{\rho_2 C_2 (1 + S_2 U_p / C_2)}{\rho_1 C_1 (1 + S_1 U_p / C_1)} = \frac{Z_{02}}{Z_{01}} [1 + U_p (1/C_2 - 1/C_1)]. \quad (19)$$

Z_{02} and Z_{01} are acoustic impedances of the two materials. To find its trend with increasing U_p , we consider two different situations.

Case 1: $C_2 > C_1$, Eq. (19) in this case reduces to

$$Z_R = \frac{Z_{02}}{Z_{01}} \left[1 - \frac{\Delta C}{C_1 C_2} U_p \right], \quad \Delta C = C_2 - C_1, \quad (20)$$

indicating a negative slope of Z_R vs U_p curve. This decreasing trend of shock impedance with rise in U_p applies to paraffin based compositions.

Case 2: For $C_1 > C_2$ Eq. (19) can be rewritten as

$$Z_R = \frac{Z_{02}}{Z_{01}} \left[1 + \frac{\Delta C}{C_1 C_2} U_p \right], \quad \Delta C = C_1 - C_2. \quad (21)$$

Equation (21) shows a rising feature of Z_R with U_p . This is the situation for four other compositions displayed in Fig. 9.

VII. HYDRODYNAMICS IN ONE DIMENSION

There exists a number of theoretical methods for physics design of dynamic compression experiments, prediction of compression induced thermodynamic changes as well as time history analysis of macroscopic flow variables. This includes (i) hydrodynamic simulation in Lagrangian/Eulerian formulation, (ii) back integration method, and (iii) newly-developed iterative characteristic method [77]. Continuum modeling of compressible fluid dynamics as encountered in hydrodynamic simulation provides an excellent platform for analyzing shock and ICE. Hydrodynamic simulation involves solving three conservation relations of mass, momentum, and energy along with material EOS applicable for a wide range of pressure and energy.

As is known that impact of flyer plates with diameter much larger than its thickness induces uniaxial strain, hence one would be interested in quantities along the axis of shock

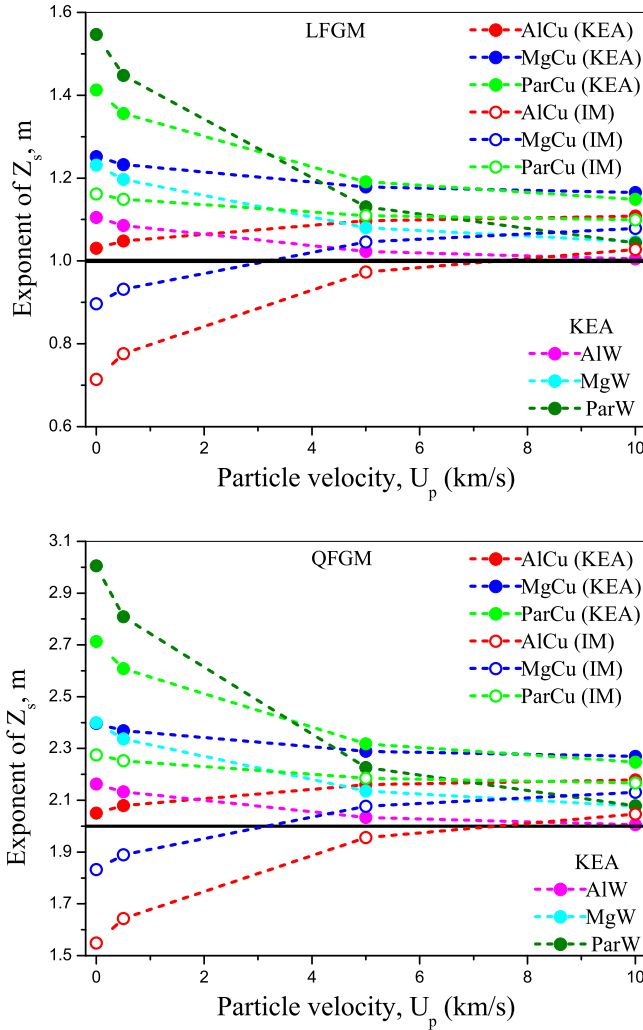


FIG. 8. Particle velocity dependence of exponent m . Filled and open circles refer to KEA and IM model based data. The dashed lines in the figure are a guide for the eye.

propagation. Deformation that initiates away from the axis due to wave propagation in lateral directions is relatively less important. Under this scenario, 1D simulation serves a good purpose. Moreover, 1D code provides good information about most of the physics involved for systems with nearly symmetric configurations. All simulations in this work have been carried out using our earlier developed 1D finite difference, explicit, Lagrangian hydrodynamic code [9,33].

For the numerical solution of conservation equations we have adopted the staggered mesh configuration of finite difference time domain method. For smearing of strong shock, we have used the Von-Neumann [78] form of artificial viscosity q given in the following form:

$$q = C_q^2 \rho \left(\frac{\partial u_x}{\partial x} \right)^2 (\Delta x)^2, \quad (22)$$

where C_q (≈ 2) is a dimensionless constant related to the number of meshes over which shock is smeared out and ρ is the fluid density. In the above x , Δx , and $u_x = \partial x / \partial t$ represent position coordinate in the direction of motion, grid spacing,

and fluid velocity at that position, respectively. Artificial viscosity is zero for $\frac{\partial u_x}{\partial x} \geq 0$.

A. Validation of hydrodynamic model: Simulation of ramp compression by Al-Cu alternate layer GDI

For validation of our hydrodynamic model and parameters, first we simulate ramp compression generated by blGDI as reported in Ref. [57]. GDI used in that experiment is composed of 200 alternating layers of Al and Cu (100 Al-Cu bilayers) with their respective thicknesses decreasing and increasing so as to change molar composition by 1% between two consecutive layers in a thickness of $d = 340$ nm. Thus total thickness of GDI considered is $D = 100d = 34 \mu\text{m}$. Following configuration of the above experiment, our simulation system consists of blGDI sandwiched between $2 \mu\text{m}$ Al and $5.5 \mu\text{m}$ Cu at the front and rear end, respectively. Beyond Cu layer, there is another $10 \mu\text{m}$ Al. Schematics of the blGDI impact induced simulation system is illustrated in the top panel of Fig. 10. In the present subsection B and A corresponds to Cu and Al, respectively. Spatial density profile would consist of vertical lines limiting between 2.71 gm/cc (Al) and 8.93 gm/cc (Cu), however, with gradually increasing width for Cu and reverse for Al.

In the following, we derive an expression for layer thickness of individual materials within any bilayer of a given GDI. This can be generalized for any number of bilayers as well as for any arbitrary material combinations.

To that end, we assume densities of two bilayer components as ρ_1 and ρ_2 ($\rho_1 < \rho_2$). Let w be the percentage change in molar composition between two successive bilayers so that $y = w/100$ is the fractional change of the same. First and last bilayers are considered to be pure materials of width d . If $d_1^{(2)}$ and $d_2^{(2)}$ are the respective widths of two materials in the second bilayer then we have

$$1 - \frac{\rho_1 d_1^{(2)} / A_1}{\rho_1 d_1^{(2)} / A_1 + \rho_2 d_2^{(2)} / A_2} = y, \quad (23)$$

where A_1, A_2 are the atomic/molar mass of two materials involved. Superscript '(2)' is used to indicate the second bilayer. Since for every bilayer $d = d_1 + d_2$ is a constant, we can replace $d_2^{(2)}$ by $d - d_1^{(2)}$ and rewrite Eq. (23) as

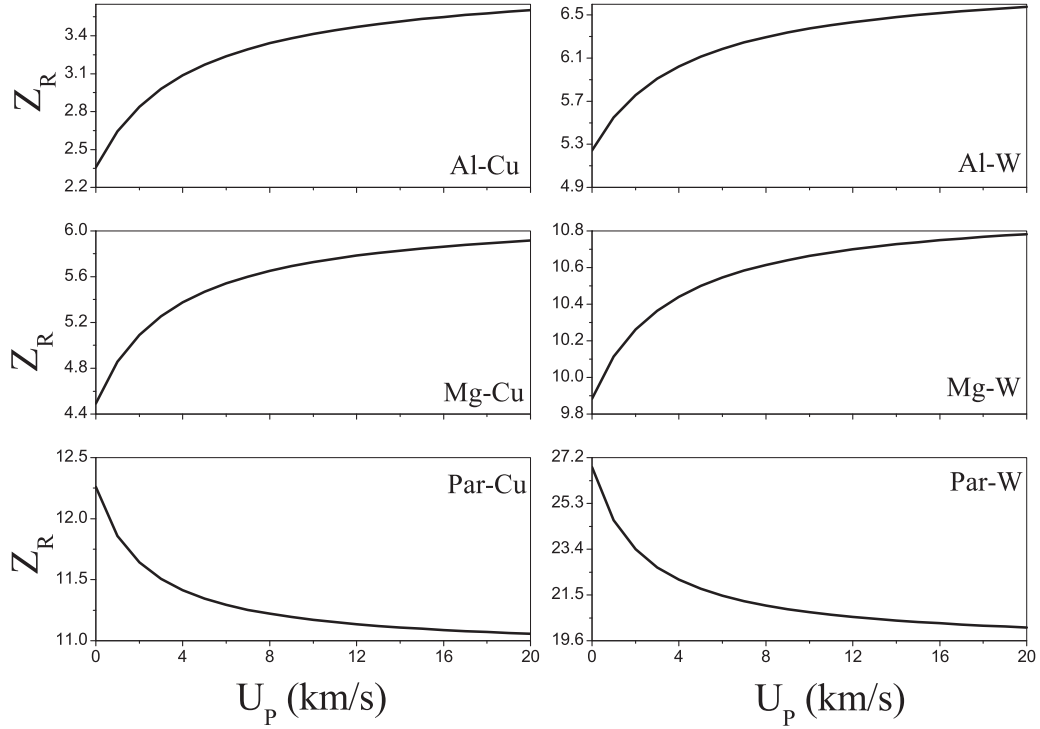
$$1 - \frac{\rho_2 A_1}{\rho_1 A_2} + \frac{\rho_2 A_1}{\rho_1 A_2} \frac{d}{d_1^{(2)}} = \frac{1}{1 - y}. \quad (24)$$

Equation (24) can be solved to arrive at

$$\frac{d}{d_1^{(2)}} = \frac{\rho_1 A_2}{\rho_2 A_1} \frac{y}{1 - y} + 1. \quad (25)$$

Thus with known value of bilayer width d , the width of the first material in the second bilayer, $d_1^{(2)}$ can be obtained from Eq. (25). Similarly between the second and third bilayers we have

$$\frac{\rho_1 d_1^{(2)} / A_1}{\rho_1 d_1^{(2)} / A_1 + \rho_2 d_2^{(2)} / A_2} - \frac{\rho_1 d_1^{(3)} / A_1}{\rho_1 d_1^{(3)} / A_1 + \rho_2 d_2^{(3)} / A_2} = y. \quad (26)$$

FIG. 9. Variation of Z_R with U_p .

Now using Eq. (23), we replace the first term by $(1 - y)$ and simplify Eq. (26) to:

$$\frac{\rho_1 d_1^{(3)}/A_1}{\rho_1 d_1^{(3)}/A_1 + \rho_2 d_2^{(3)}/A_2} = (1 - y) - y = 1 - 2y. \quad (27)$$

On use of $d_2^{(3)} = d - d_1^{(3)}$, we get the width of the first material in the third bilayer as

$$\frac{d}{d_1^{(3)}} = \frac{\rho_1 A_2}{\rho_2 A_1} \frac{2y}{1 - 2y} + 1. \quad (28)$$

The method can be applied between any n th and $(n + 1)$ th bilayers to find the width of the first material in the $(n + 1)$ th bilayer. Thus generalizing Eq. (28) we get

$$\frac{d}{d_1^{(n+1)}} = \frac{\rho_1 A_2}{\rho_2 A_1} \frac{ny}{1 - ny} + 1 = R \left[\frac{1}{1 - ny} - 1 \right] + 1, \quad (29)$$

where $R = \rho_1 A_2 / \rho_2 A_1$. Thus width of the first material is indirectly proportional to R and number of bilayers n . Further, d_1 decreases continuously in progressing from low density end to high density end; however, it will never become zero. In our code, we imposed the last bilayer to be pure high density material, making $d_1^{(n+1)} = 0$. The magnitude of R depends on bilayer material parameters, namely density and atomic/molar mass. For Al-Cu, Mg-Cu, and Par-Cu compositions $R = 0.7$, 0.52 , and 0.017 , respectively. For a GDI with a given number of bilayers, depletion in thickness of low density material would be maximum for Al-Cu, then Mg-Cu and very low for Par-Cu. Too small value of R does not allow appreciable change in width of the first material as in the case of Par-Cu. It can be shown that the fractional change in span

of first material between two consecutive bilayers is

$$\Delta d^{(n)} = 1 - \frac{d_1^{(n+1)}}{d_1^{(n)}} = \frac{Ry}{[1 - ny][1 - (n + 1)y + (n + 1)Ry]}. \quad (30)$$

For $\Delta d^{(n)}$ to be the same as change in molar fraction y , R should satisfy the approximate relation:

$$R \approx \frac{1 - (n + 1)y}{1 - ny} \approx 1. \quad (31)$$

In writing the above we have neglected terms of the order y^2 ($y = 0.01$ in Ref. [57] and has been followed here). For Cu based GDI, the value of R will be close to 1, if Li is used as low density component. The above derivation would help in predicting the effectiveness of any arbitrary composition bilayer GDI in ramp compression experiment.

For numerical simulation of bGDI/bFGM induced impact cases we have considered 200 Lagrangian meshes within $34 \mu\text{m}$ GDI/FGM. Thus the smallest mesh size for Al and Cu layers are 4.7 nm and 2.34 nm in the case of Al-Cu GDI. Mesh size for other supporting materials is chosen in such a way that Z_0 per mesh is close to $0.1 \text{ gm/cm}^2/\mu\text{s}$. This resulted in sufficient reduction of numerical oscillations at an interface of dissimilar materials. To minimize the spurious numerical oscillations of hydrodynamic variables, C_q is chosen to be 2.45 thereby spreading the shock front over approximately six meshes.

The expression given in Eq. (29) has been introduced in our hydro code for generating bGDI with any given B-A combination and any number of bilayers. Assigning EOS parameters for each monolayer is done simultaneously. First, we simulate the experiment of Ref. [57], i.e., Al-Cu impactor

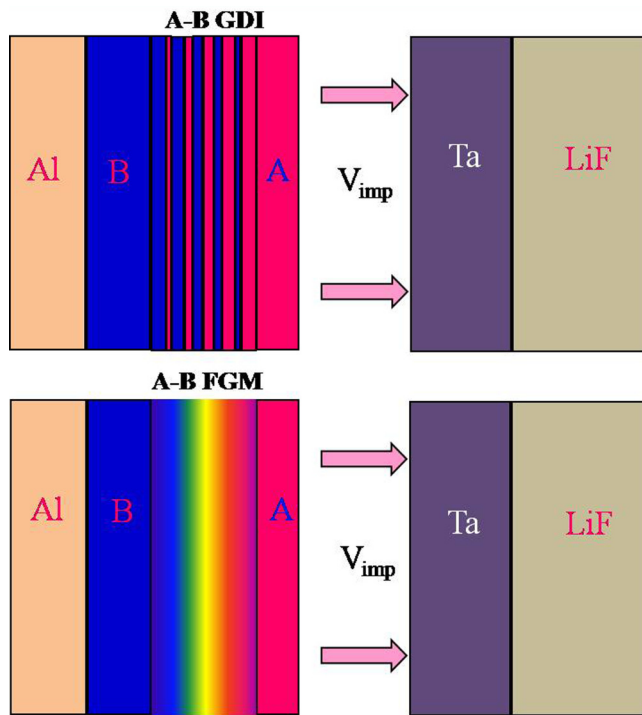


FIG. 10. Schematic diagram of ramp simulation system. Bilayer GDI (top) and binary FGM (bottom) plate ($34 \mu\text{m}$) with composition A-B, impacting at velocity V_{imp} onto a LiF-backed $43 \mu\text{m}$ Ta target. Impactor is sandwiched between $5.5 \mu\text{m}$ B plate and $2 \mu\text{m}$ A plate. Simulation results with Cu/W as B and paraffin, Mg and Al as A are compared here for ramp compression.

assembly loaded onto a $43 \mu\text{m}$ thick Ta target at two different impact velocities of 4.055 and 3.01 km/s. Pressure histories at Ta-GDI interface generated by our code (solid lines) along with simulation results of Ref. [57] (dashed lines) for $V_{\text{imp}} = 4.055 \text{ km/s}$ are shown in Fig. 11(a). Very good agreement of pressure waveform as well as peak values can be observed between the two. Time profiles of pressure show an initial shock jump to 0.83 and 0.52 Mbar followed by a linear ramping up to 7 ns and 8.5 ns for higher and lower impact velocities, respectively. Moreover, peak pressures achieved in our simulation, i.e., 1.53 and 1.0 Mbar agree very well with the experimental values, as provided in Table VIII. It is worth mentioning here that the *quoted value of impact velocity, i.e., 4.6 km/s shown in Fig. 7 of Ref. [57] could be an error.* Maximum pressure (1.0 Mbar) achieved in our simulation for $V_{\text{imp}} = 3.01 \text{ km/s}$ is the same as reported in Ref. [57].

Particle velocity at target-impactor interface shown by solid lines of Fig. 11(b) for the two impact cases follow the same profile as stress. A corresponding profile as reported in Ref. [57] is plotted in the dashed curve. Overall good agreement can be observed for pulse shape as well as peak velocity. Maximum fluid velocity for two loading cases is 1.67 and 1.23 km/s in our simulation.

Finally, particle velocity histories at Ta-LiF interface obtained from our code, along with experimental results of Ref. [57], are presented in Fig. 11(c). Maximum fluid velocities at target rear end (2.52 and 1.91 km/s) are in excellent agreement with experiment (dashed lines). The difference in

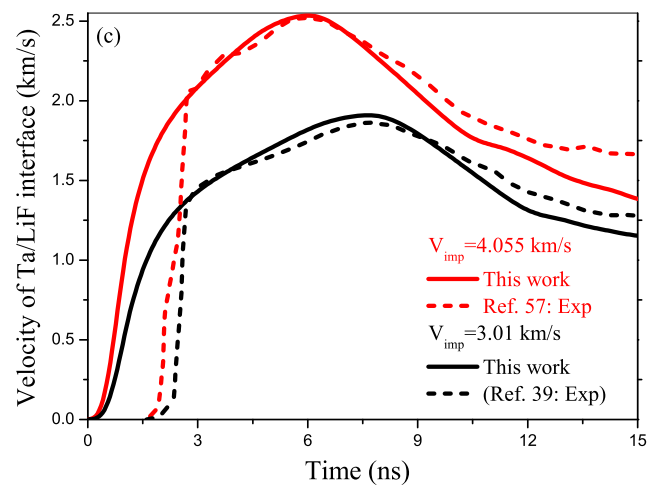
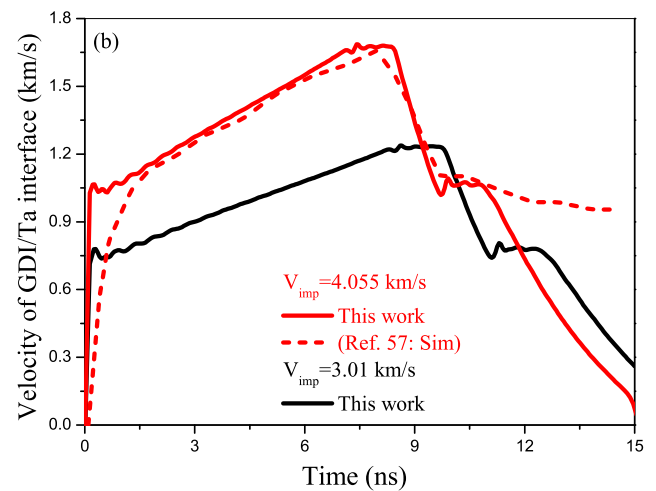
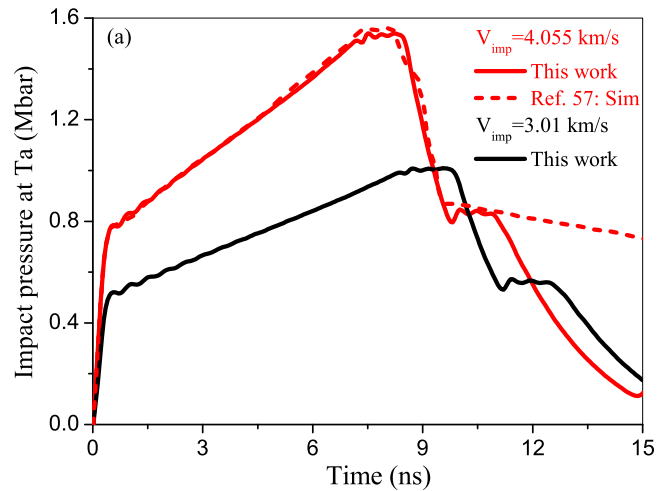


FIG. 11. Time histories of: (a) Ta target pressure, (b) particle velocities at GDI-Ta interface, and (c) particle velocity at Ta-LiF interface for impact at 4.055 km/s (red) and 3.01 km/s (black). Solid lines in each case correspond to our simulation, whereas dashed lines refer to Ref. [57].

shock arrival time from experiment was also observed in ALEGRA simulation of Ref. [57].

TABLE VIII. Results summary of bIGDI simulation and comparison with Ref. [57].

Impact velocity (km/s)	Impact pressure (Mbar)	Peak pressure (Mbar)	Ref.
4.055	0.80	1.51	Ref. [57] Sim.
	0.83	1.53	This work
3.01	0.52	0.99	Ref. [57] Sim.
	0.52	1.0	This work

Results demonstrated in Fig. 11 show excellent agreement between our 1D simulation and those reported in Ref. [57] thereby validating our model and code for analyzing such experiments. Results also indicate that for target-impactor diameter ratio used in the experiment, 3D effects are not playing a significant role in altering shock wave properties.

In the current work we extend our simulation study for different B/A combinations and propose possible situations that would generate ramp compression with better isentropic characteristics. For each combination, bIGDI induced ramp profiles will be compared with analogous bFGM.

VIII. BINARY FGM FOR RAMP COMPRESSION

We will now utilize bFGM for generating ramp waves in a simulation setup equivalent to the above experiment. To that end, bIGDI is replaced by either type of bFGM as shown in the bottom panel of Fig. 10. Following Ref. [57], first we consider impact at 4.055 km/s. All calculations were carried out considering bFGM consisting of 200 individual layers (numerical mesh) each of thickness 170 nm. Accordingly, the time step was chosen to be a picosecond or less for realizing smooth variation of physical parameters with time.

A. Ramp generation by Al-Cu FGM: Comparison with Al-Cu GDI

Pressure pulse generated at Ta target due to impact of Al-Cu bFGM is shown in Fig. 12(a). Time profile for LFGM shows initial shock pressure of magnitude 0.8 Mbar due to impact of 2 μm Al, followed by a gradual rise of pressure to reach the maximum value of 1.5 Mbar in about 7.2 ns and a steady hold before a sharp decline in pressure occurs. Pressure profile in the ramping zone is parallel to that of Al-Cu GDI. In the case of QFGM, after initial shock pressure rise is rather slow making the trajectory placed below both LFGM and GDI. As time progresses, pressure increases at a faster rate eventually crossing both the other curves.

Spatial variation of shock impedance has direct influence on ramp profile for FGM induced cases. In order to establish the correlation between the two, we have fitted the ramping zone of Fig. 12(a) with a generalized power law function of time given below,

$$P(t) = P_H + P_R \left(\frac{t - t_i}{t_f - t_i} \right)^n. \quad (32)$$

In the above t_i and t_f correspond to the times when onset of ramping and saturation occur while n is the nonlinear exponent of time. P_H is shock pressure due to impact of low density

front material. Reducing shock impedance of front material will result in lower value of P_H . P_R refers to net pressure rise from base shock level, i.e., $P_R = P(t_f) - P(t_i)$. Fitted curves (dashed lines) are shown in the inset of Fig. 12(a). The values of n are 0.77 and 1.59 for LFGM and QFGM, respectively, indicating pressure to be a sublinear/subquadratic function of time. In contrast, pressure rises almost linearly ($n = 1.02$) for bIGDI.

Particle velocities at Ta-LiF interface for Al-Cu bFGMs, shown in blue and green curves of Fig. 12(b), follow the same profile as GDI. Ramp generation by other binary FGMs will be studied in the next subsection.

B. Effect of impedance ratio on ramp profile: Binary FGM vs bilayer GDI

In Sec. VI B we have seen that shock impedance ratio Z_R is lowest for the Al-Cu system, and it increases as the density of one component is lowered. Here we explore the influence of Z_R on ramp pressure produced by Mg-Cu and Par-Cu FGM. Corresponding target pressures are shown in Figs. 12(c) and 12(e) with results for equivalent bIGDI superimposing on them. In making Mg-Cu or Par-Cu bIGDI, molar composition of Mg or paraffin has been increased by 1% between two successive bilayers. The effect of Mg as low impedance material is to reduce initial shock pressure P_H from 0.83 Mbar for the Al-Cu system to 0.51 Mbar. With paraffin as one component of bFGM, P_H has further reduced to 0.28 Mbar. This reduction is expected to minimize shock induced entropy production as discussed in later sections. Since peak pressure is the same in all three cases, parameter Z_R has significant influence on the ramping part of pressure rise, i.e., P_R .

It can be noticed that ramping slope for the Mg-Cu system has changed significantly for the GDI case by making it concave upwards (superlinear). Particle velocity histories for Mg-Cu based GDI/FGM obey similar characteristics as the Al-Cu system.

In contrast to FGM cases, Par-Cu alternating layer GDI delivered shock pressure of 0.28 Mbar lasting for about 6 ns when another strong shock overtakes it to raise the final pressure to 1.2 Mbar. Thus bIGDI involving low impedance but high molar mass material launches two successive shocks with a finite time gap that inhibits ramp formation. The reason behind this can be easily understood by the following observation. A larger molecular mass of paraffin wax, 374 gm/mol as compared to 63.5 gm of Cu, leads to very small value of R and hence $\Delta d^{(n)}$, thereby not allowing the width of the paraffin layer to change adequately. This eventually turns GDI into a two-layer (a thick paraffin and thinner Cu layer) impactor. The signatures of two separate shock waves are quite prominent in particle velocity history for Par-Cu bIGDI as displayed in curve (f) of Fig. 12. Using any kind of polymer based materials, e.g., PE, PMMA, TPX, etc. with still larger molar mass would not be of any help.

C. Enhancing peak ramp pressure: Binary FGM vs bilayer GDI

For many HEDP applications we require investigation of EOS properties at high dynamic pressures. Moreover,

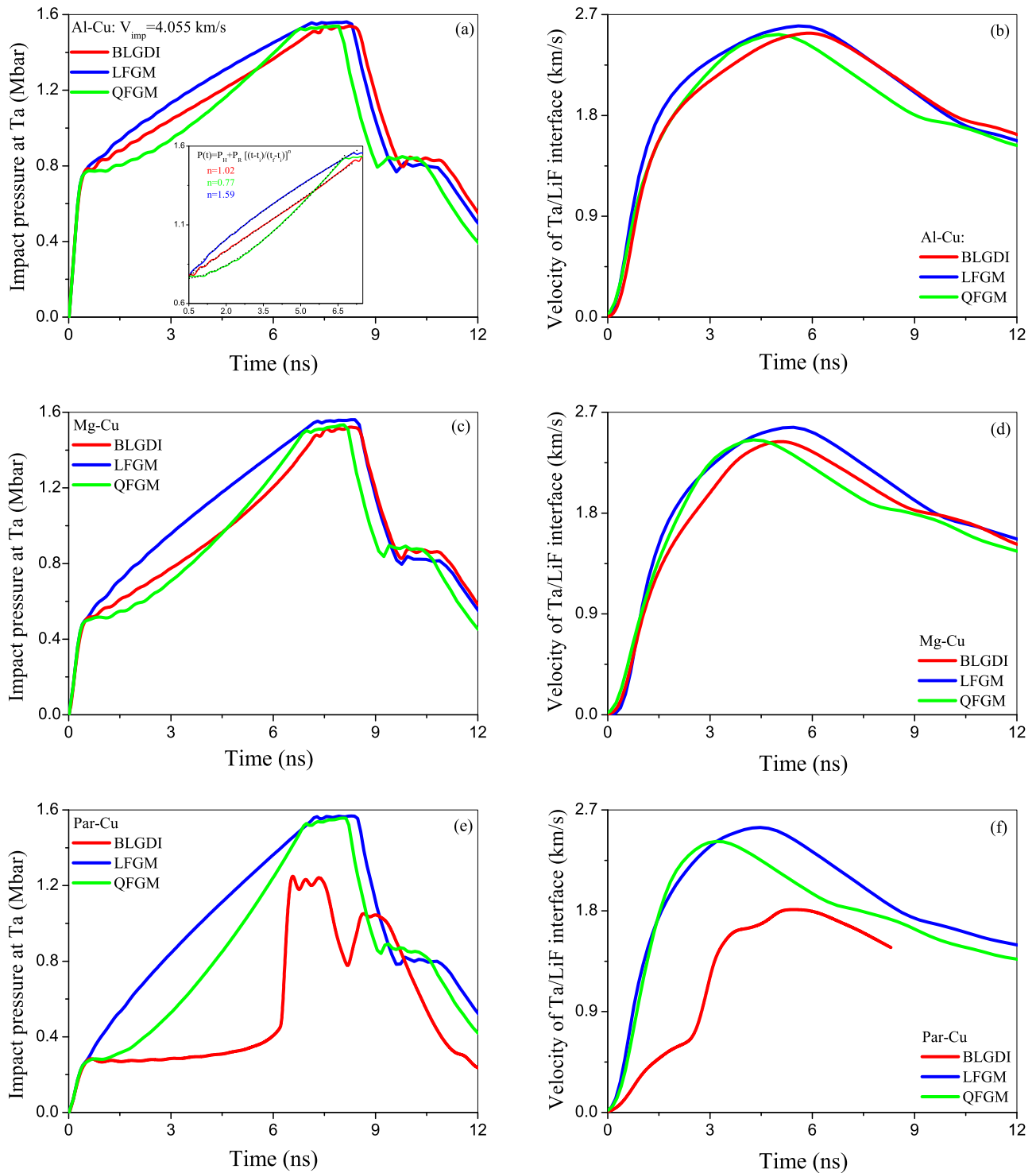


FIG. 12. Simulation results for time variation of Ta pressure [(a), (c), (e)] and particle velocity at Ta-LiF interface [(b), (d), (f)] generated by three Cu based FGM and GDI plates. Inset of (a) shows the fitting of ramp pressure with Eq. (32).

experimental investigation of shock induced elastic-plastic transition, plasticity, etc., particularly at extremely high strain rates, are difficult due to limited range of ramp pressure. In order to make such studies feasible within commonly available experimental techniques, one needs to enhance peak ramp pressures. With this motivation, we have replaced Cu

of bLGDI/bFGM with high impedance material W. Three W based systems, namely Al-W, Mg-W, and Par-W have been considered for this purpose. Shock impedance ratio of these binary mixtures is more than that of Cu based analogous mixtures. The configuration of simulation system is the same as in Fig. 10, except that the back end of GDI/FGM is now

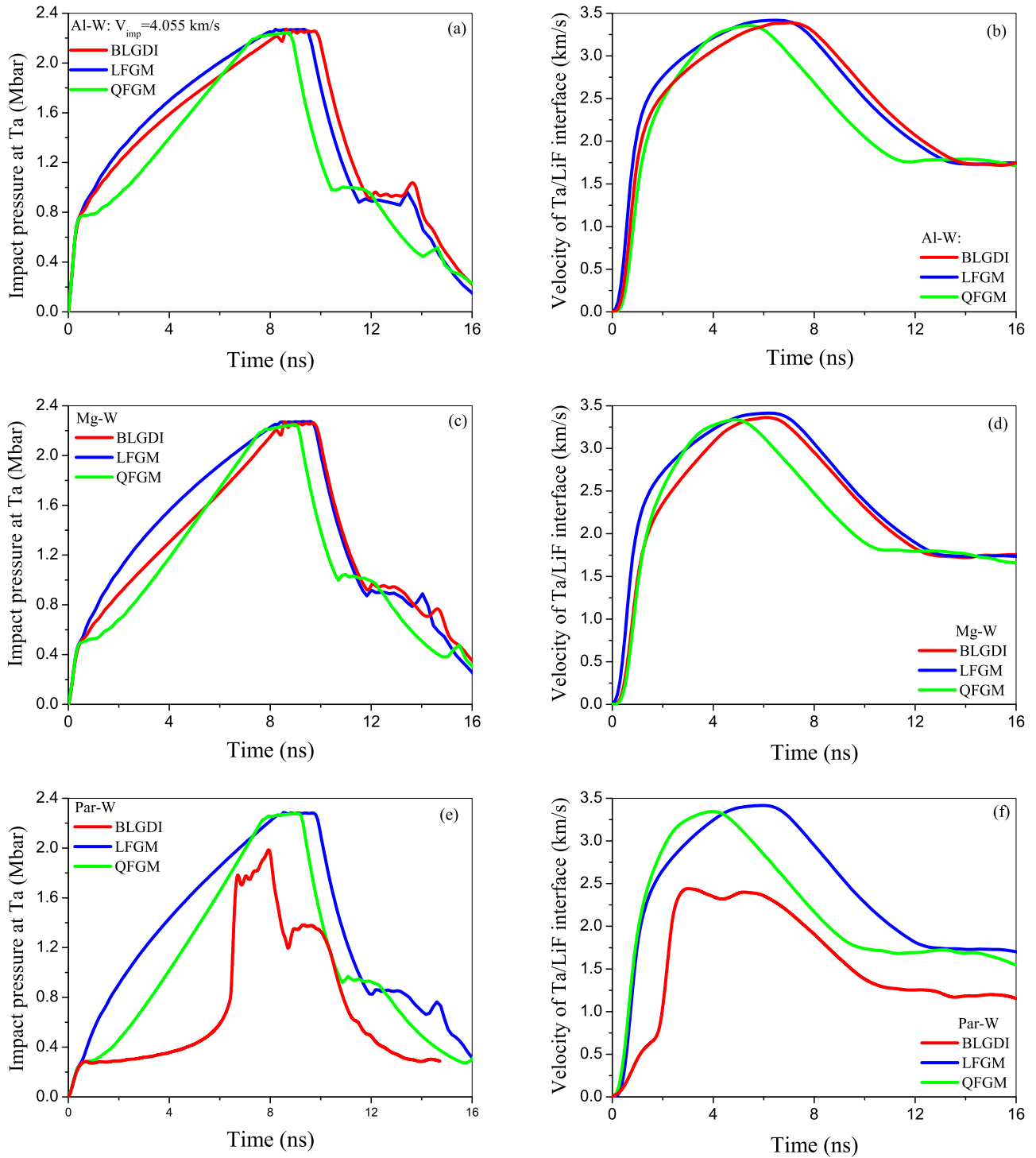


FIG. 13. Simulation results for time variation of pressure at Ta-GDI interface due to impact of (a) Al-W, (c) Mg-W, (e) Par-W LFGM, QFGM, and GDI at 4.055 km/s. Corresponding particle velocities at the Ta-LiF interface are shown in curves (b), (d), and (f).

W. The front end has Al/Mg/Paraffin as in the case of the Cu based system.

In Fig. 13 we have demonstrated the ramp pressure pulse generated in 43 μm Ta target by 34 μm thick bIGDI or bFGM (L/Q) when impacted at 4.055 km/s. As expected, the shock pressure part P_H for Al-W (a), Mg-W (b), and Par-W (c) systems remains the same as the corresponding Cu based cases.

However, the final pressure has increased from 1.5 Mbar to 2.26 Mbar, almost 50% increase. This increase in ramp part of total pressure is caused due to nearly 100% increase in the value of Z_R as shown in Fig. 9.

In the case of bIGDI with paraffin as the front layer we observe the same two shock structures as in the Par-Cu case. However, peak pressure has increased to about 1.7 Mbar.

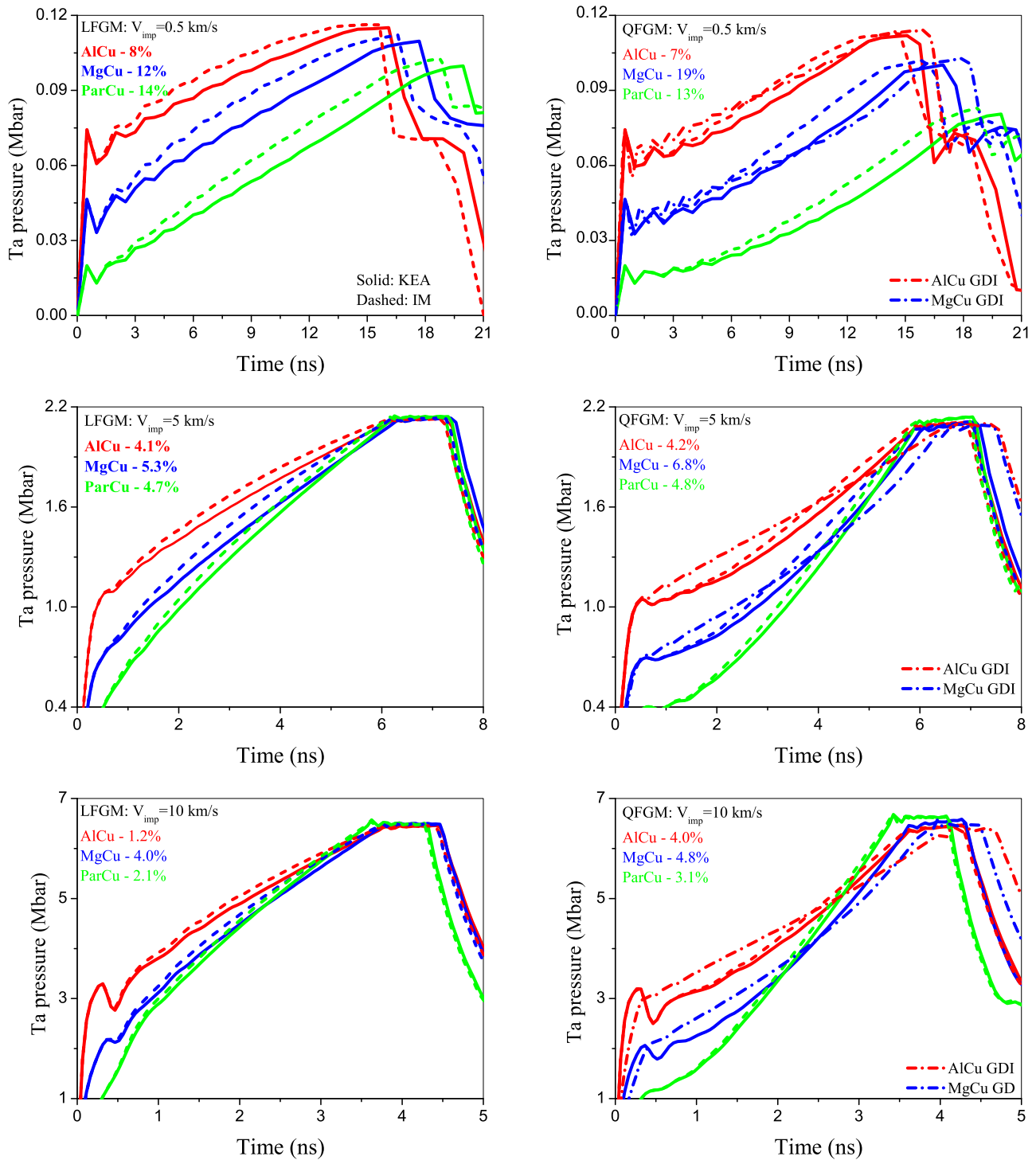


FIG. 14. Time history of Ta pressure produced by Cu based bFGM/bIGDI for three different impact velocities. Solid curves are the estimations based on KEA model while dashed curves represent IM results. Bilayer GDI results are shown as a dashed-dotted curve along with QFGM results.

D. Effect of increasing impact velocity

It is well known that peak ramp pressure can be raised by impacting the target at higher velocity. In the case of graded density impactor (either discrete or continuous) increasing impact velocity significantly influences ramp profile also. This has been investigated in this section. Since com-

pression dynamics for paraffin based GDI is better represented by two successive shocks, Par-Cu and Par-W GDI have not been considered for further study of ramp generation. Time histories of pressure at Ta target due to impact by three Cu based FGM/GDI at $V_{imp} = 0.5, 5.0, \text{ and } 10.0$ km/s are shown in Fig. 14. It is evident that for low velocity impact ($V_{imp} = 0.5$ km/s), spread in peak pressures among various FGMs

TABLE IX. Coefficients (P_R and n) of fitting function Eq. (32) for bFGM and bIGDI impact at 0.5 km/s. Shock pressure P_H can be determined exactly and hence not shown.

Impactor	GDI		Model	LFGM		QFGM	
	P_R	n		P_R	n	P_R	n
Al-Cu	0.049	1.07	KEA	0.051	0.93	0.048	1.67
			IM	0.056	0.71	0.054	1.44
Mg-Cu	0.059	1.70	KEA	0.067	0.95	0.60	1.67
			IM	0.079	0.74	0.065	1.44
Par-Cu			KEA	0.087	0.93	0.062	1.84
			IM	0.086	0.93	0.064	1.65

is large with maximum and minimum pressure occurring for Al-Cu and Par-Cu, respectively. Spread in peak values reduces for higher impact velocities. Corresponding GDI cases (displayed along with QFGM) are comparable with LFGM results. Average pulse widths are about 21, 11, and 6 ns for three impact velocities, respectively.

The above study demonstrates that as V_{imp} is increased, both the shock and ramp part of pressure increases. For all the impact cases shock part of total pressure is highest for Al-Cu and least for Par-Cu FGM. Interestingly shock to ramp ratio reduces for Par-Cu FGM cases thereby making shock jump less important for very high velocity impact (10 km/s) as shown in Fig. 14.

For quantitative comparison of pressure profile generated by three Cu based impactors we have fitted the pressure in the ramping zone with power law relation given by Eq. (32). The fitting coefficients, namely P_R and n for $V_{\text{imp}} = 0.5$ km/s as obtained with KEA and IM models of mixture EOS, are listed in Table IX. Values of exponent n for all three impact velocities ($V_{\text{imp}} = 0.5, 5.0,$ and 10.0 km/s) as obtained by KEA model are compared in Fig. 15. It can be noticed that pressure rise is marginally superlinear for Al-Cu GDI and is less influenced by impact strength. Pressure rise is superlinear for Mg-Cu GDI and the value of n drops when V_{imp} is increased beyond 0.5 km/s. For all LFGM cases ramp pressure rise is sublinear ($n < 1$). Except for Al-Cu LFGM, n decreases continuously as V_{imp} is increased. Subquadratic ($1 < n < 2$) time variation of ramp pressure is observed for all QFGMs. Magnitude of n continuously reduces for Par-Cu QFGM. To sum up, we conclude that superlinear/superquadratic variation of Z_s with layer position induces ramp pressure which is sublinear/subquadratic in time. The reduction in magnitude of exponent is expected as spatial variation of C does not follow the same monotonic function as Z_s .

Now, differentiating Eq. (32) w.r.t time we get

$$\frac{dP(t)}{dt} = \frac{nP_R}{t_f - t_i} \left[\frac{t - t_i}{t_f - t_i} \right]^{n-1}. \quad (33)$$

Equation (33) indicates that rate of change of pressure is not constant. Steepness of pressure profile at saturation, i.e., at $t = t_f$ is given by $\frac{nP_R}{t_f - t_i}$. Intercomparison of this parameter among six different types of FGMs and two GDIs is shown in the bar graph of Fig. 15. For all the FGM/GDI combinations a sharp increase in this parameter can be observed when impact

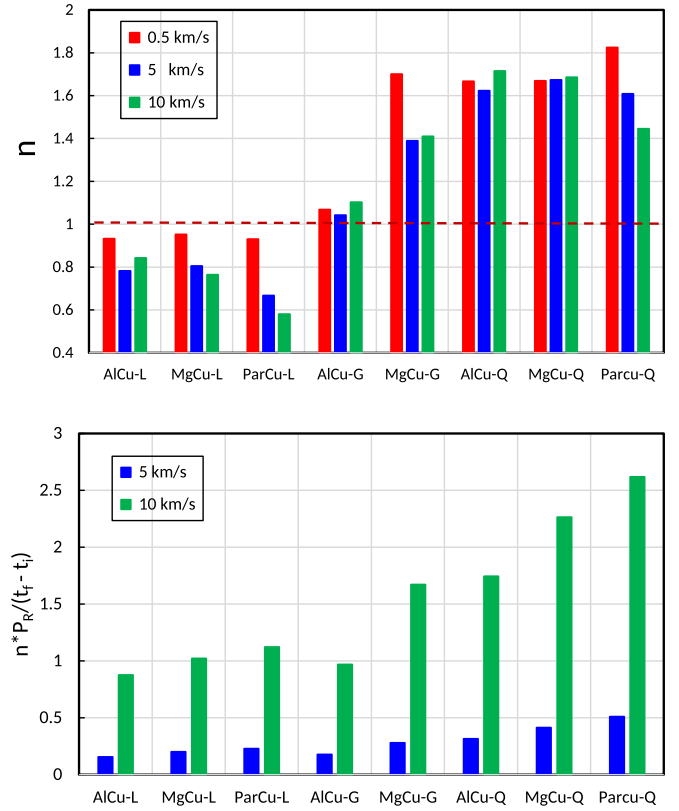


FIG. 15. Comparison of parameters affecting rate of pressure increase in the ramping zone among different bFGM and bIGDI. Top and bottom panel display exponent of power law and slope of $P(t)$ vs t curve at the final time when saturation in pressure is reached.

velocity is changed from 5.0 km/s to 10.0 km/s. Steepness parameters for $V_{\text{imp}} = 0.5$ km/s are one order less in magnitude and hence are not shown. Further, for a particular impact velocity and binary composition rate of pressure rise is lowest for LFGM, followed by GDI and maximum for QFGM. This is expected as the slope of $P(t)$ vs t curve for QFGM is very low at the onset of ramping.

Outcome of increasing impact strength for W based FGM/GDI cases are demonstrated in Fig. 16. The following observations can be made from the results of low velocity impact (0.5 km/s): (i) impact by both LFGM and QFGM results in continuously decreasing peak pressures from the Al-W system to the Par-W one, (ii) for a particular composition, peak pressures achieved in QFGMs are lower than LFGM cases and a significant difference is noticed for Par-W FGM, (iii) peak pressure due to impact by Al-W GDI is comparable with Al-W LFGM whereas for Mg-W GDI it is comparable with Mg-W QFGM. Impact at higher velocities lead to comparable pressures for all three W based FGMs as well as GDI cases.

E. Effect of EOS model on ramp pressure profile

Next, we investigate the effect of FGM EOS model on isentropic generation. In previous sections we have shown that even though there exists appreciable difference in C vs ρ curves for Cu based bFGMs obtained by two different models,

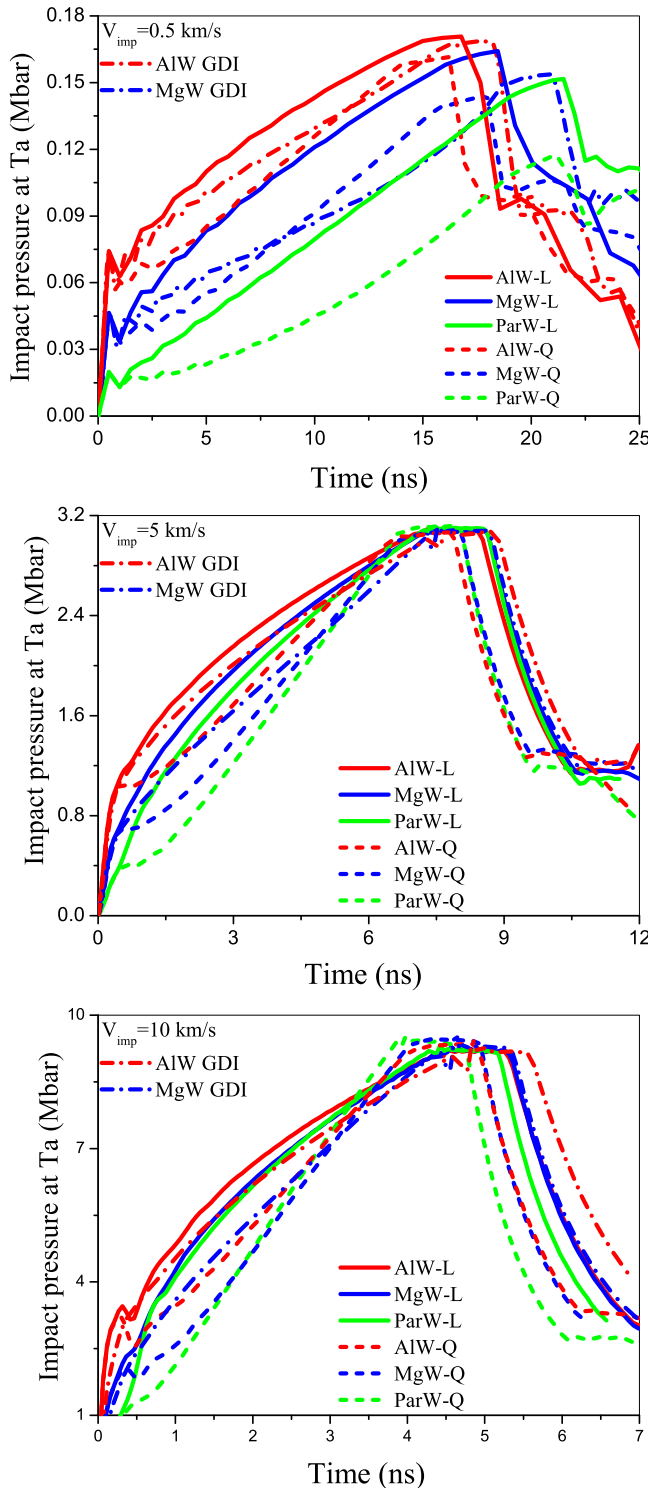


FIG. 16. Effect of impact velocity on ramp profile generated by three W based composite impactors.

but the same is not reflected that significantly in the shock impedance profile. The primary reason for this is the large difference in densities of the two components used in FGM. To study this effect we have considered three impact cases with velocities 0.5 km/s, 5 km/s, and 10 km/s as shown in Fig. 14. In all the curves solid lines refer to the KEA EOS model whereas dashed lines are the results of the IM model.

For each case the maximum percentage difference in ramp pressures obtained by two models are displayed in Fig. 14. From the results we infer that (i) the IM model predicts a higher value of pressure in the ramping zone than the KEA model indicating influence of the EOS model, (ii) the difference in pressure-time trajectory between the two models is the maximum for low velocity impact, and it gradually decreases for elevated launch velocities, (iii) for the Mg-Cu system, deviation is always more for QFGM cases, (iv) minimum and maximum percentage difference is observed for Al-Cu and Mg-Cu combinations, respectively, but there is no appreciable difference in peak pressure values obtained by KEA and IM models.

Study indicates that for designing the impactor for hypervelocity launch, the mixture EOS model does not play a significant role, but it does influence low velocity impact. For the sake of completeness, ramp profile parameters P_R and n corresponding to $V_{\text{imp}} = 0.5$ km/s obtained with IM and KEA models are compared in Table IX. Even though overall feature, i.e., sublinear/superlinear dependence of pressure with time remains the same for both the models, IM predicts a lower rate of pressure rise as compared to the KEA model.

IX. CHARACTERISTICS OF ISENTROPES GENERATED BY BINARY FGM AND BILAYER GDI

In this section, we make quantitative study of Ta isentropes generated by impact of different composition bFGM/blGDI. This has been realized by comprehensive study of thermodynamic parameters such as peak pressure P_{max} , maximum compression ρ/ρ_0 , temperature rise T , and change in entropy from ideal isentrope in units of C_V , $\Delta S/C_V$ as a function of impact strength. In obtaining T and $\Delta S/C_V$ we have followed the methodology of Ref. [33]. The consolidated results for Cu based bFGM/blGDI are presented in Table X. As discussed in earlier sections that difference between the KEA and IM model is maximum for low impact strength, hence influence of the EOS model on target thermodynamics has been examined for the $V_{\text{imp}} = 0.5$ km/s case only. Target thermodynamics for isentropes generated by W based FGM/GDI cases are presented in Table XI. To distinguish the adiabats generated by bFGM/blGDI from strong shocks, huginiot states corresponding to the same compression ratio are presented.

The following observations can be made from the above two tables.

(i) For very low velocity impact, even though maximum difference in ramp pressure between KEA and IM models is as large as 19%, the same is not that severe for target heating and entropy generation.

(ii) Larger compression associated with least target heating and entropy production can be achieved by QFGM and hence serves better. Performance of the Al based blGDI is comparable with LFGM, whereas the Mg based one is better than LFGM.

(iii) For a given impact, maximum and minimum temperature rise occur for composite impactors with Al and paraffin as low density component, respectively. Since Par-Cu/Par-W GDI lead to shock compression as shown in Fig. 12 and Fig. 13, the corresponding results for target thermodynamics are not listed here.

TABLE X. Comparison of Ta target compression parameters for Cu based bFGM and bIGDI.

Impactor	Model	P_{\max} (Mbar)	ρ/ρ_0	T_{\max} (K)	$\Delta S/C_V$
$V_{\text{imp}} = 0.5 \text{ km/s}$					
Hugoniot		0.11	1.06	341.5	2.0×10^{-2}
AlCu-GDI		0.11	1.06	337.2	7.6×10^{-3}
LFGM	KEA	0.11	1.06	337.2	7.1×10^{-3}
	IM	0.12	1.06	337.8	7.2×10^{-3}
QFGM	KEA	0.11	1.06	336.3	7.0×10^{-3}
	IM	0.11	1.06	336.5	7.0×10^{-3}
MgCu-GDI		0.10	1.05	331.8	2.1×10^{-3}
LFGM	KEA	0.11	1.06	333.9	2.1×10^{-3}
	IM	0.11	1.06	334.7	2.1×10^{-3}
QFGM	KEA	0.10	1.05	331.3	2.0×10^{-3}
	IM	0.10	1.05	331.9	2.0×10^{-3}
ParCu-L	KEA	0.10	1.05	330.6	2.1×10^{-4}
	IM	0.10	1.05	331.5	2.2×10^{-4}
ParCu-Q	KEA	0.08	1.04	324.9	2.0×10^{-4}
	IM	0.08	1.04	325.5	2.0×10^{-4}
$V_{\text{imp}} = 5.0 \text{ km/s}$					
Hugoniot		2.53	1.59	9279	2.69
AlCu-GDI		2.10	1.57	2740	1.49
LFGM	KEA	2.13	1.57	2778	1.50
QFGM	KEA	2.10	1.57	2630	1.45
MgCu-GDI		2.04	1.56	1629	0.97
LFGM	KEA	2.13	1.58	1735	1.02
QFGM	KEA	2.11	1.58	1568	0.92
ParCu-L	KEA	2.14	1.59	1202	0.65
ParCu-Q	KEA	2.14	1.59	947	0.41
$V_{\text{imp}} = 10.0 \text{ km/s}$					
Hugoniot		9.95	2.12	7.6×10^4	4.49
AlCu-GDI		6.41	2.05	1.7×10^4	3.00
LFGM	KEA	6.44	2.05	1.7×10^4	3.02
QFGM	KEA	6.45	2.05	1.6×10^4	2.96
MgCu-GDI		6.52	2.08	1.0×10^4	2.51
LFGM	KEA	6.48	2.08	1.1×10^4	2.58
QFGM	KEA	6.55	2.09	9111	2.37
ParCu-L	KEA	6.50	2.08	1.1×10^4	2.53
ParCu-Q	KEA	6.62	2.12	4889	1.74

(iv) One order increase in impact velocity from 0.5 km/s to 5.0 km/s corresponds to entropy change by two orders in magnitude. However, entropy rise is not that significant for impact at 10 km/s. This can be explained by noticing that maximum change in entropy takes place due to initial shock compression, and entropy remains practically constant in the ramping zone where pressure is raised isentropically.

For illustration, in Fig. 17 we have demonstrated shock-ramp adiabats of Ta target generated by Cu and W based bFGM/bIGDI impacted at 10 km/s. We also compare target temperature and entropy rise for six different FGM cases with those of analogous GDI.

Top panel of Fig. 17 shows that there is no appreciable difference between compression curves generated by different FGMs and GDI. Initial shock jump in pressure can be identified from the point of intersection of hugoniot with isentropes as shown in the inset of Cu based results. The intersection occurs at low pressures for low impedance front material.

TABLE XI. Comparison of Ta target compression parameters for W based bFGM and bIGDI.

Impactor	Model	P_{\max} (Mbar)	ρ/ρ_0	T_{\max} (K)	$\Delta S/C_V$
$V_{\text{imp}} = 0.5 \text{ km/s}$					
Hugoniot		0.17	1.08	369.0	5.5×10^{-2}
AlW-GDI		0.17	1.08	352.1	7.8×10^{-3}
LFGM		0.17	1.08	352.3	7.4×10^{-3}
QFGM		0.16	1.08	349.8	7.1×10^{-3}
MgW-GDI		0.15	1.08	346.4	2.3×10^{-3}
LFGM		0.16	1.08	348.8	2.2×10^{-3}
QFGM		0.14	1.07	343.3	2.0×10^{-3}
ParW-L		0.15	1.08	345.1	1.8×10^{-4}
ParW-Q		0.12	1.06	335.9	2.2×10^{-4}
$V_{\text{imp}} = 5.0 \text{ km/s}$					
Hugoniot		3.97	1.75	1.9×10^4	3.31
AlW-GDI		3.09	1.73	3382	1.60
LFGM		3.08	1.72	3437	1.60
QFGM		3.07	1.73	2972	1.45
MgW-GDI		3.10	1.74	2080	1.09
LGM		3.09	1.73	2330	1.20
QFGM		3.08	1.74	1781	0.93
ParW-L		3.10	1.74	1936	1.02
ParW-Q		3.11	1.75	1100	0.45
$V_{\text{imp}} = 10.0 \text{ km/s}$					
Hugoniot		15.65	2.32	1.4×10^5	5.0
AlW-GDI		9.35	2.27	2.2×10^4	3.16
LGM		9.18	2.26	2.1×10^4	3.14
QFGM		9.30	2.28	1.8×10^4	2.96
MgW-GDI		9.08	2.27	1.5×10^4	2.78
LGM		9.22	2.27	1.6×10^4	2.88
QFGM		9.41	2.31	1.0×10^4	2.40
ParW-L		9.24	2.27	1.9×10^4	3.04
ParW-Q		9.41	2.32	7.3×10^3	2.05

Intercomparison of $P - \rho/\rho_0$ adiabats arising from different bFGM/bIGDI can be found in the inset of W based curves.

Temperature rise and entropy change is much lower for all cases of bFGM/bIGDI than hugoniot. GDI produces more entropy than corresponding QFGM. This is not surprising as each bilayer is supposed to generate two successive shocks due to impact of two stand-alone materials with appreciable difference in their shock impedance. Ramp profiling is the outcome of thickness arrangements. Binary FGM, particularly QFGM, not only generates ramp profile but also guarantees lower temperature rise and lower entropy production for same peak pressure. Thus among two types of bFGM, the quadratic one serves better for the current shock-ramp compression experiment. The study establishes our earlier observation [33] that QFGM, even though technologically challenging to fabricate, provides a thermodynamically superior isentropic state. Comparing the performance of W based compositions with that of Cu based ones, it is observed that higher compression can be achieved in the former without significant change in temperature and entropy.

Finally, in Fig. 18 we compare entropy change in Ta target due to impact by different types of graded materials

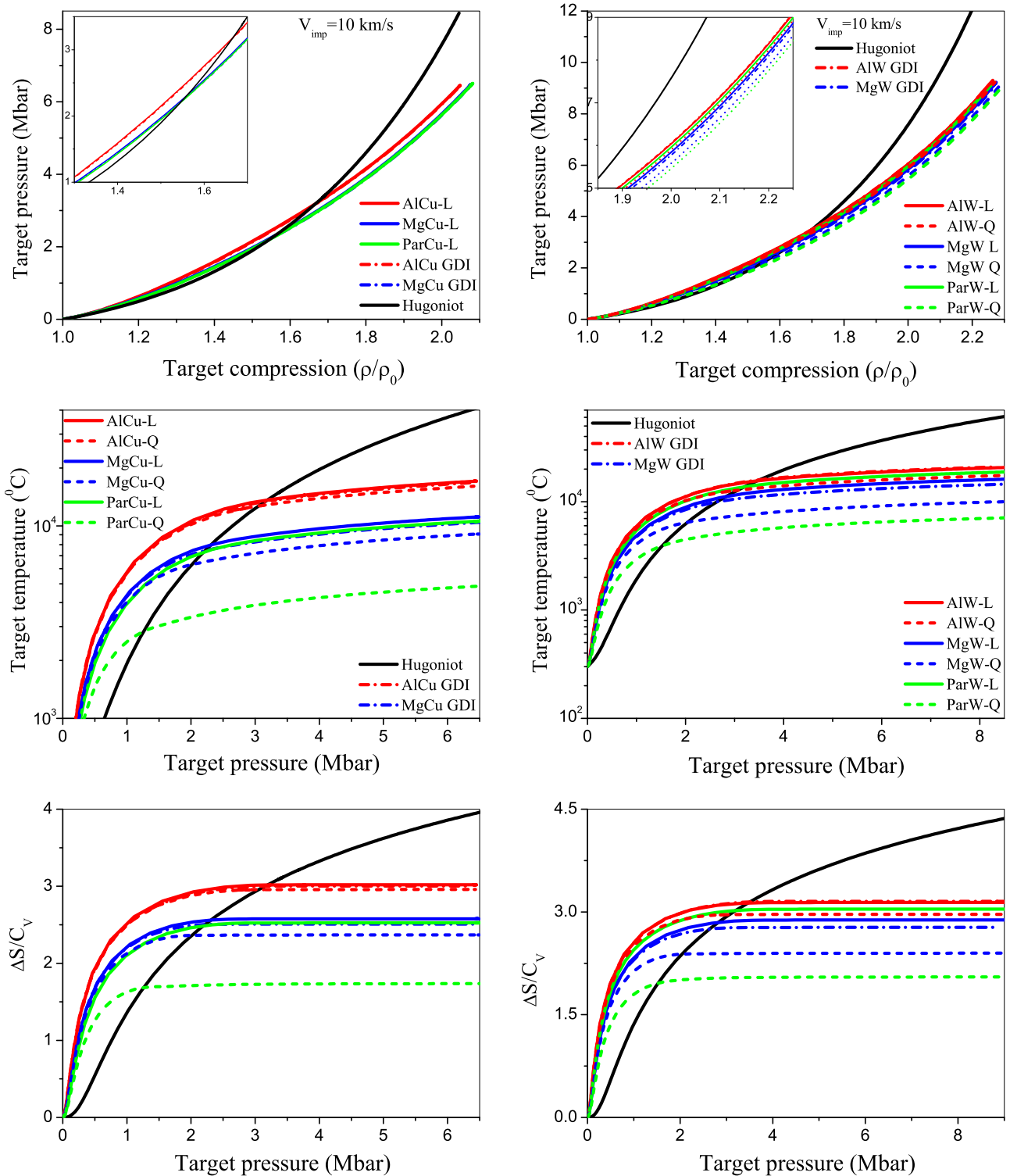


FIG. 17. Comparison of thermodynamic parameters of Ta target in respect to different bFGM/bLGD impact at 10 km/s. Top panel shows $P - \rho/\rho_0$ isentropes generated. Pressure dependent temperature rise and entropy change (in units of C_v) are displayed in middle and bottom panels, respectively. Solid and dashed lines correspond to LFGM and QFGM, respectively, whereas dashed-dotted lines refer to bLGD. For better comparison of the quality of isentropes generated we have overlaid the corresponding hugoniot results.

at 5.0 km/s and 10.0 km/s. Although compression for the W based composite impactor is more (1.75 and 2.27 for $V_{\text{imp}} = 5$ and 10 km/s) than Cu based composite impactors (1.56 and 2.08, respectively), entropies are almost compar-

able for both the cases. Entropy changes for Al based GDI are nearly comparable with Al based LFGM whereas the same for Mg based GDI fall between LFGM and QFGM. The bar graph brings out the important observation that

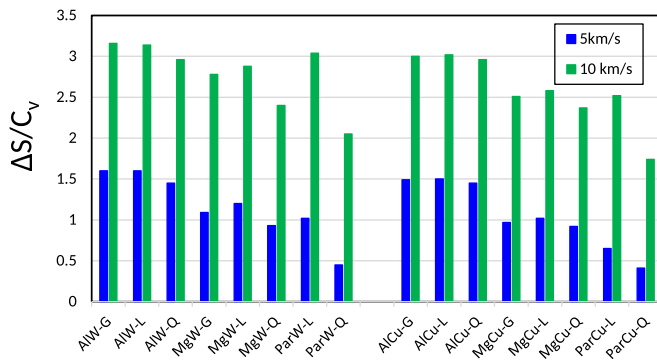


FIG. 18. Bar graph showing the comparison of entropy generated in Ta target due to impact by different bIGDI and bFGM at velocity 5 km/s (blue) and 10 km/s (green).

entropy change is least for QFGM with paraffin as one component.

X. CONCLUSIONS

We report development of KEA model based code for determining EOS of material mixtures. The code is utilized for constructing analytical functions for density dependence of EOS parameters, namely sound velocity and hughoniot slope for different concentration material mixtures. Sound velocity for six binary mixtures, viz., Al-Cu, Mg-Cu, Par-Cu, Al-W, Mg-W, and Par-W, is found to be minimum at certain density. Analogous functions obtained by com-

monly used IM model do not exhibit such minima, thereby proving it to be inadequate for determining accurate EOS of mixtures.

Analytical functions are utilized for developing generalized Mie-Grüneisen EOS that incorporates anisotropic feature of FGM (linear and quadratic) through position dependent hughoniot parameters. Power law relations are proposed for position dependent shock impedance of different FGMs. It is shown that linear/quadratic variation of density along thickness gives rise to superlinear/superquadratic spatial profile of shock impedance.

Hydrodynamic simulations are performed to generate ramp compression in Ta target by constant velocity impact of thus constructed bFGMs. Further, pressure pulse generated by different bFGM revealed that time profile of pressure pulse is a direct consequence of spatial profile of shock impedance. The study is thus useful in selecting components of bFGM and their layering sequence for achieving required pulse shape of ICE.

Thermodynamic characteristics of target compression parameters, e.g., maximum pressure, temperature rise, and entropy production have been investigated in order to search for isentropic dynamics close to ideal one. It is shown that larger compression associated with least target heating and entropy production can be achieved by QFGM, making it a better choice for impactor. Our study provides a comprehensive assessment of effectiveness of different bFGMs and their analogous bIGDI in generating thermodynamically consistent isentropic waves.

- [1] R. P. Drake, *High Energy Density Physics: Fundamentals, Inertial Fusion, and Experimental Astrophysics* (Springer, New York, 2006).
- [2] Y. B. Zeldovich, Y. P. Raizer, *Physics of Shock Waves and High Temperature Hydrodynamic Phenomena* (Dover, New York, 2002).
- [3] B. A. Remington, R. E. Rudd, and J. S. Wark, From microjoules to megajoules and kilobars to gigabars: probing matter at extreme states of deformation, *Phys. Plasmas* **22**, 090501 (2015).
- [4] K. Lorenz, M. Edwards, A. Jankowski, S. Pollaine, R. Smith, and B. Remington, High pressure, quasi-isentropic compression experiments on the Omega laser, *High Ener. Dens. Phys.* **2**, 113 (2006).
- [5] J. Edwards, K. Lorenz, B. Remington, S. Pollaine, J. Colvin, B. F. L. D. Braun, D. Reisman, J. McNaney, J. A. Greenough, R. Wallace, H. Louis, and D. Kalantar, Laser-Driven Plasma Loader for Shockless Compression and Acceleration of Samples in the Solid State, *Phys. Rev. Lett.* **92**, 075002 (2004).
- [6] R. F. Smith, S. M. Pollaine, S. J. Moon, K. T. Lorenz, P. M. Celliers, J. H. Eggert, H. Park, and G. Collins, High planarity x-ray drive for ultrafast shockless-compression experiments, *Phys. Plasmas* **14**, 057105 (2007).
- [7] T. S. Duffy and R. F. Smith, Ultra-High Pressure Dynamic Compression of Geological Materials, *Front. Earth Sci.* **7**, 23 (2019).
- [8] D. C. Swift, R. G. Kraus, E. Loomis, D. G. Hicks, J. M. McNaney, and R. P. Johnson, Shock formation and the ideal shape of ramp compression waves, *Phys. Rev. E* **78**, 066115 (2008).
- [9] A. Ray and S. V. G. Menon, Quasi-isentropic compression using functionally graded materials in gas gun and explosive driven systems, *J. Appl. Phys.* **105**, 064501 (2009).
- [10] L. M. Barker and R. E. Hollenbach, Shock-Wave studies of PMMA, fused silica, and sapphire, *J. Appl. Phys.* **41**, 4208 (1970).
- [11] L. V. Altshuler, R. F. Trunin, K. K. Krupnikov, and N. V. Panov, *Phys. Usp.* **39**, 539 (1996).
- [12] D. B. Hayes, C. A. Hall, J. R. Asay, M. D. Knudson, Measurement of the compression isentrope for 6061-T6 aluminum to 185 GPa and 46% volumetric strain using pulsed magnetic loading, *J. Appl. Phys.* **96**, 5520 (2004).
- [13] J.-P. Davis, Experimental measurement of the principal isentrope for aluminum 6061-T6 to 240 GPa, *J. Appl. Phys.* **99**, 103512 (2006).
- [14] R. W. Lemke, M. D. Knudson, and J.-P. Davis, Magnetically driven hyper-velocity launch capability at the Sandia Z accelerator, *Int. J. Impact. Eng.* **38**, 480 (2011).
- [15] C. A. Hall, J. R. Asay, M. D. Knudson, W. A. Stygar, R. B. Spielman, and T. D. Pointon D. B. Reisman, A. Toor, and R. C. Cauble, Experimental configuration for isentropic compression of solids using pulsed magnetic loading, *Rev. Sci. Instrum.* **72**, 3587 (2001).

- [16] R. S. Hawke, D. E. Duerre, J. G. Huebel, H. Klapper, D. J. Steinberg, and R. N. Keeler, Method of isentropically compressing materials to several megabars, *J. Appl. Phys.* **43**, 2734 (1972)
- [17] R. E. Kidder, Theory of homogeneous isentropic compression and its application to laser fusion, *Nucl. Fusion* **14**, 53 (1974).
- [18] D. C. Swift and R. P. Johnson, Quasi-isentropic compression by ablative laser loading: Response of materials to dynamic loading on nanosecond time scales, *Phys. Rev. E* **71**, 066401 (2005).
- [19] N. Amadou, E. Brambrink, A. Benuzzi-Mounaix, G. Huser, F. Guyot, S. Mazevet, G. Morard, T. de Resseguier, T. Vinci, K. Myanishi, N. Ozaki, R. Kodama, T. Boehly, O. Henry, D. Raffestin, M. Koenig, Direct laser-driven ramp compression studies of iron: A first step toward the reproduction of planetary core conditions, *High Ener. Dens. Phys.* **9**, 243 (2013).
- [20] J. K. Wicks, R. F. Smith, D. E. Fratanduono, F. Coppari, R. G. Kraus, M. G. Newman, J. Ryan Rygg, J. H. Eggert, T. S. Duffy, Crystal structure and equation of state of Fe-Si alloys at super-Earth core conditions, *Sci. Adv.* **4**, eaao5864 (2018).
- [21] D. N. Polsin, D. E. Fratanduono, J. R. Rygg, A. Lazicki, R. F. Smith, J. H. Eggert, M. C. Gregor, B. J. Henderson, X. Gong, J. A. Delettrez, R. G. Kraus, P. M. Celliers, F. Coppari, D. C. Swift, C. A. McCoy, C. T. Seagle, J.-P. Davis, S. J. Burns, G. W. Collins, and T. R. Boehly, X-ray diffraction of ramp-compressed aluminum to 475 GPa, *Phys. Plasmas* **25**, 082709 (2018).
- [22] R. F. Smith, D. E. Fratanduono, D. G. Braun, T. S. Duffy, J. K. Wicks, P. M. Celliers, S. J. Ali, A. Fernandez-Pañella, R. G. Kraus, D. C. Swift, G. W. Collins, and J. H. Eggert, Equation of state of iron under core conditions of large rocky exoplanets, *Nat. Astron.* **2**, 452 (2018).
- [23] J. Wang, F. Coppari, R. F. Smith, J. H. Eggert, A. E. Lazicki, D. E. Fratanduono, J. Ryan Rygg, T. R. Boehly, G. W. Collins, and T. S. Duffy, X-ray diffraction of molybdenum under ramp compression to 1 TPa, *Phys. Rev. B* **94**, 104102 (2016).
- [24] J. Wang, R. F. Smith, J. H. Eggert, D. G. Braun, T. R. Boehly, J. R. Patterson, P. M. Celliers, R. Jeanloz, G. W. Collins, and T. S. Duffy, Ramp compression of iron to 273 GPa, *J. Appl. Phys.* **114**, 023513 (2013).
- [25] D. E. Fratanduono, T. R. Boehly, P. M. Celliers, M. A. Barrios, J. H. Eggert, R. F. Smith, D. G. Hicks, G. W. Collins, D. D. Meyerhofer, The direct measurement of ablation pressure driven by 351-nm laser radiation, *J. Appl. Phys.* **110**, 073110 (2011).
- [26] D. E. Fratanduono, R. F. Smith, S. J. Ali, D. G. Braun, A. Fernandez-Pañella, S. Zhang, R. G. Kraus, F. Coppari, J. M. McNaney, M. C. Marshall, L. E. Kirch, D. C. Swift, M. Millot, J. K. Wicks, and J. H. Eggert, Probing the Solid Phase of Noble Metal Copper at Terapascal Conditions, *Phys. Rev. Lett.* **124**, 015701 (2020).
- [27] J. H. Eggert, R. F. Smith, D. C. Swift, R. E. Rudd, D. E. Fratanduono, D. G. Braun, J. A. Hawreliak, J. M. McNaney, and G. W. Collin, Ramp compression of tantalum to 330 GPa, *High Pres. Res.* **35**, 339 (2015).
- [28] Q. Xue, S. Jiang, Z. Wang, F. Wang, X. Zhao, and Y. Ding, Laser pulse shape design for laser-indirect-driven quasi-isentropic compression experiments, *AIP Adv.* **8**, 025202 (2018).
- [29] R. F. Smith, J. H. Eggert, R. Jeanloz, T. S. Duffy, D. G. Braun, J. R. Patterson, R. E. Rudd, J. Biener, A. E. Lazicki, A. V. Hamza, J. Wang, T. Braun, L. X. Benedict, P. M. Celliers, and G. W. Collins, Ramp compression of diamond to five terapascals, *Nature (London)* **511**, 330 (2014).
- [30] Gently compressing materials to record levels, Science and Technology Review, Lawrence Livermore National Laboratory, Livermore, CA, USA, September, 2019.
- [31] D. Batani, A. Balducci, D. Beretta, A. Bernardinello, T. Lower, M. Koenig, A. Benuzzi, B. Faral, and T. Hall, Equation of state data for gold in the pressure range <10 TPa, *Phys. Rev. B* **61**, 9287 (2000).
- [32] A. Benuzzi-Mounaix, M. Koenig, G. Huser, B. Faral, D. Batani, E. Henry, M. Tomasini, B. Marchet, T. A. Hall, M. Boustie, T. de Resseguier, M. Hallouin, F. Guyot, D. Andrault, and T. Charpin, Absolute equation of state measurements of iron using laser driven shocks, *Phys. Plasmas* **9**, 2466 (2002).
- [33] A. Ray and S. V. G. Menon, Hydrodynamic simulation and thermodynamic characterization of functionally graded material induced isentropic compression: Towards optimum density profile, *J. Appl. Phys.* **110**, 024905 (2011).
- [34] X. Wang, C. Dai, Q. Wang, L. Hao, J. Bai, Y. Yu, Q. Wu, H. Tan, J. Hu, G. Luo, Q. Shen, L. Zhang, Development of a three-stage gas gun launcher for ultrahigh-pressure Hugoniot measurements, *Rev. Sci. Instrum.* **90**, 013903 (2019).
- [35] L. C. Chhabildas, L. N. Kmetyk, W. D. Reinhart, and C. A. Hall, Enhanced hypervelocity launcher-capabilities to 16 km/s, *Int. J. Impact Engg.* **17**, 183 (1995).
- [36] T. F. Thornhill, L. C. Chhabildas, W. D. Reinhart, D. L. Davidson, Particle launch to 19 km/s for micro-meteoroid simulation using enhanced three-stage light gas gun hypervelocity launcher techniques, *Int. J. Impact Engg.* **33**, 799 (2006).
- [37] W. D. Reinhart, L. C. Chhabildas, D. E. Carroll, T. K. Bergstresser, T. F. Thornhill, N. A. Winfree, Equation of state measurements of materials using a three-stage gun to impact velocities of 11 km/s, *Int. J. Impact Engg.* **26**, 625 (2006)
- [38] A. Ray and A. Singla (unpublished).
- [39] M. D. Furnish, M. Kipp, W. D. Reinhart, T. J. Vogler, W. W. Anderson, and R. S. Hixson, Exploring pulse shaping for Z using graded-density impactors on gas guns, Technical Report SAND2005-6210, Sandia National Laboratories, Albuquerque NM, 2005.
- [40] A. Ray, Generation of isentropic compression by use of multi-layer composite flyer and its influence on system thermodynamics: A simulation study, *J. Phys.: Conf. Ser.* **500**, 152011 (2014).
- [41] L. C. Chhabildas, L. M. Barker, J. R. Asay, and T. G. Trucano, Relationship of fragment size to normalized spall strength for materials, *Int. J. Impact Engg.* **10**, 107 (1990).
- [42] L. C. Chhabildas and J. R. Asay, *Dynamic Yield Strength and Spall Strength Measurements under Quasi-Isentropic Loading, in Shock Waves and High-Strain-Rate Phenomena in Materials*, edited by M. A. Meyers, L. E. Murr, and K. P. Staudhammer (Marcel Dekker, New York, 1992), pp. 947–955.
- [43] L. M. Barker, High-pressure, quasi-isentropic impact experiments, in *Shock Waves in Condensed Matter*, edited by J. R. Asay, R. A. Graham, and G. K. Straub (Elsevier, New York, 1984).
- [44] L. C. Chhabildas, L. M. Barker, J. R. Asay, T. G. Trucano, G. I. Kerley, and J. E. Durra, Launch capabilities to over 10 km/s, *Shock Waves in Condensed Matter*, edited by S. C. Schmidt,

- R. D. Dick, J. W. Forbes, and D. G. Tasker (Elsevier Science Publishers, 1992), pp. 1025–1031.
- [45] L. C. Chhabildas, J. E. Dunn, W. D. Reinhart, and J. M. Miller, An impact technique to accelerate flier plates to velocities over 12 km/s, *Int. J. Impact Engg.* **14**, 121 (1993).
- [46] J. Nguyen, New Routes to High Temperatures and Pressures, *Science and Technology Review* LLNL, Livermore, CA, USA (2007).
- [47] R. T. Krone, L. P. Martin, J. R. Patterson, D. Orlikowski, and J. H. Nguyen, Fabrication and characterization of graded impedance impactors for gas gun experiments from hot-pressed magnesium and polyethylene powders, *Mater. Sci. Engg. A* **479**, 300 (2008).
- [48] J. P. Kelly, J. H. Nguyen, J. Lind, M. C. Akin, B. J. Fix, C. K. Saw, E. R. White, W. O. Greene, P. D. Asimow, and J. J. Haslam, Application of Al-Cu-W-Ta graded density impactors in dynamic ramp compression experiments, *J. Appl. Phys.* **125**, 145902 (2019).
- [49] U. Leushake, A. N. Winter, B. H. Rabin, and B. A. Corff, General Aspects of FGM Fabrication by Powder Stacking, *Mater. Sci. Forum.* **308**, 6311 (1999).
- [50] Y. Miyamoto, W. A. Kaysser, B. H. Rabin, A. Kawasaki, and R. G. Ford, *Functionally Graded Materials: Design, Processing and Applications* (Springer Science, New York, 1999).
- [51] B. R. Marple and J. Boulanger, Graded casting of materials with continuous gradients, *J. Am. Ceram. Soc.* **77**, 2747 (2005).
- [52] A. C. Hall, C. W. Weyant, J. L. Wise, C. A. Hall, S. C. Jones, D. A. Urrea, J. F. McCloskey, J. W. Cates, T. J. Roemer, A. J. Mayer, D. E. Beatty, Sandia Report, SAND2005-7690C.
- [53] J. H. Nguyen, D. Orlikowski, F. H. Streitz, J. A. Moriarty, and N. C. Holmes, High-pressure tailored compression: Controlled thermodynamic paths, *J. Appl. Phys.* **100**, 023508 (2006).
- [54] L. P. Martin, J. R. Patterson, D. Orlikowski, and J. H. Nguyen, Application of tape-cast graded impedance impactors for light-gas gun experiments, *J. Appl. Phys.* **102**, 023507 (2007).
- [55] M. Naebe, K. Shirvanimoghaddam, Functionally graded materials: A review of fabrication and properties, *Appl. Mat. Today* **5**, 223 (2016).
- [56] B. Kieback, A. Neubrand, H. Riedel, Processing techniques for functionally graded materials, *Mat. Sci. Engg. A* **362**, 81 (2003).
- [57] J. L. Brown, D. P. Adams, C. S. Alexander, J. L. Wise, and M. B. Prime, Estimates of Ta strength at ultrahigh pressures and strain rates using thin-film graded-density impactors, *Phys. Rev. B* **99**, 214105 (2019).
- [58] G. E. Duvall and S. M. Taylor, Shock parameters in a two component mixture, *J. Compos. Mater.* **5**, 130 (1971).
- [59] J. L. Jordan, and M. R. Baer, Mixture model for determination of shock equation of state, *J. Appl. Phys.* **111**, 083516 (2012).
- [60] D. Eakins and N. N. Thadhani, Discrete particle simulation of shock wave propagation in a binary Ni+Al powder mixture, *J. Appl. Phys.* **101**, 043508 (2007).
- [61] O. E. Petel, F. X. Jette, Comparison of methods for calculating the shock hughoniot of mixtures, *Shock Waves* **20**, 73 (2010).
- [62] A. Ray, M. K. Srivastava, G. Kondayya, and S. V. G. Menon, Improved equation of state of metals in the liquid-vapor region, *Laser Par. Beams* **24**, 437 (2006).
- [63] S. S. Batsanov, *Effects of Explosions on Materials: Modification and Synthesis under High-Pressure Shock Compression* (Springer, Berlin, 1994).
- [64] R. G. McQueen, S. P. Marsh, J. N. Fritz, Hugoniot equation of state of twelve rocks, *J. Geophys. Res.* **72**, 4999 (1967).
- [65] M. A. Meyers, *Dynamic Behaviour of Materials* (John Wiley & Sons, New York, 1994).
- [66] Shock wave data base: <http://www.ihed.ras.ru/rusbank/catsearch.php>.
- [67] S. J. Yep, J. L. Belof, D. A. Orlikowski, J. H. Nguyen, Fabrication and Application of High Impedance Graded Density Impactors in Light-Gas Gun Experiments, *Rev. Sci. Instrum.* **84**, 103909 (2013).
- [68] P. Chen, G. Luo, Y. Liu, Q. Shen, and L. Zhang, Fabrication of Al-W functionally graded impact material via vacuum hot-pressing sintering method, *J. Phys.: Conf. Ser.* **419**, 012010 (2013).
- [69] L. Qiao, X. F. Zhang, Y. He, A. S. Shi, Z. W. Guan, Mesoscale simulation on the shock compression behavior of Al-W-Binder granular metal mixtures, *Materials and Design* **47**, 341 (2013).
- [70] G. Luo, J. Bai, H. Tan, Q. Shen, J. Hu, Q. Wang, C. Dai, Q. Wu, and L. Zhang, Characterizations of Mg-W System Graded-Density Impactors for Complex Loading Experiments, *Metal. Mat. Trans. A* **41**, 2389 (2010).
- [71] Y. F. Alekseev, L. V. Al'tshuler, and V. P. Krupnikova, Shock compression of two-component paraffin-tungsten mixtures, *Zhurnal Prikladnoi Mekhaniki i Tekhnicheskoi Fiziki* **4**, 152 (1971), translation available online.
- [72] G. A. Cox and J. R. Maw, Modelling the equation of state of a graded density impactor, *J. Phys.: Conf. Ser.* **500**, 142007 (2014).
- [73] P. J. Torvik, A simple theory for shock propagation in homogeneous mixtures, Air Force Institute of Technology Technical Report (1970).
- [74] H. A. Bruck, A one-dimensional model for designing functionally graded materials to manage stress waves, *Int. J. Solids and Struct.* **37**, 6383 (2000).
- [75] A. J. Markworth, K. S. Ramesh, and W. P. Parks Jr, Modelling studies applied to functionally graded materials, *J. Mat. Sci.* **30**, 2183 (1995).
- [76] G. M. Zhang and R. C. Batra, Wave propagation in functionally graded materials by modified smoothed particle hydrodynamics (MSPH) method, *J. Comp. Phys.* **222**, 374 (2007).
- [77] S. D. Rothman, J. P. Davis, J. Maw, C. M. Robinson, K. Parker, and J. Palmer, Measurement of the principal isentropes of lead and lead-antimony alloy to 400 kbar by quasi-isentropic compression, *J. Phys. D- Appl. Phys.* **38**, 733 (2005).
- [78] J. Von Neumann and R. D. Richtmyer, A method for the numerical calculations of hydrodynamic shocks, *J. Appl. Phys.* **21**, 232 (1950).